A Non-Linear Simulink Simulation Of a Large, Flexible Aircraft - FLEXSIM

by

Dr. David K. Schmidt
Monument, CO

Project Supported by

MUSYN, Inc.
Minneapolis, MN

Under Subcontract No. 001-SC01

Prime Contract
NNX12CA14C / Order # 4200428594
NASA Dryden Flight Research Center

March 17, 2013

Executive Summary

The objective of the project was to develop a public domain, nonlinear aeroelastic simulation model (The Simulation) based on the Rockwell B-1 aircraft. This simulation model is to support research being performed under the prime contract funded by the NASA Dryden Flight Research Center. Plus, The Simulation will also be made available to the public to be used as a benchmark simulation for education and research on the dynamics of flexible aircraft as well as for aeroservoelastic-system identification and control.

The mathematical models used to develop The Simulation were, for the most part, available in the open literature. But some additional aerodynamic modeling was performed, and some modifications were made to the feedback systems incorporated into The Simulation. Consequently, it is important to note that The Simulation is not intended to be a model of the actual B-1 aircraft, but rather a generic aircraft similar to the B-1.

The resulting non-linear simulation model includes all six rigid-body degrees of freedom, plus five elastic degrees of freedom; expanded aerodynamic models, including the aerodynamic coupling between the rigid-body and elastic degrees of freedom; a non-linear model of the turbojet engine dynamics and limits; models of the measurement set (sensed responses) used on the B-1; and models of the effects of atmospheric turbulence. In addition to the engine, the vehicle configuration, as modeled, includes several control effectors, including symmetric and antisymmetric horizontal tail deflections, wing spoilers, a split rudder, and forward control vanes for structural mode control.

Additionally, the stability-augmentations systems (SAS) and structural-mode-control systems (SMCS) for the B-1 are also described in the open literature. But some modifications have been made to the control laws in these systems, to better meet program objectives, and the resulting feedback systems incorporated into The Simulation. The included systems are longitudinal, lateral, and directional SAS's, and vertical and lateral SMCS's. These systems are also intended to provide benchmarks for further active-control research.

With the aerodynamic database, engine model, and feedback-system gain schedules employed, the simulation should be sufficiently valid over a rather large flight envelope. Based on testing performed to date, this envelope extends from approximately Mach 0.5 to 0.8 and

altitudes from 5000 to 30K feet, thus spanning a range of dynamic pressures. Hence The Simulation provides an extensive range of flight environments for research.

In addition to describing the models incorporated into The Simulation, this document also includes a users manual explaining how The Simulation may be initialized and executed. Plus, the results from several test cases have been included, which users may use for comparisons. It should be noted that The Simulation is a fast-time, research simulation. And hence to effectively use it, users must be familiar with both the Simulink tool itself, as well as the development of dynamic models using Simulink. The initial release of The Simulation should be considered a beta version.

Table of Contents

		Page
	Executive Summary	2
1.	Introduction and Vehicle Description	5
2.	Equations of Motion	9
	Rigid-Body Degrees of Freedom Elastic Degrees of Freedom Selection of the Vibration Modes Included Kinematic Equations	
3.	Force and Moment Models	15
	Aerodynamic Forces and Moments Propulsive Forces and Moments Generalized Forces	
4.	Measurement Set – Vehicle Responses	26
	Air-Data Set Measured Angular Rates and Accelerations	
5.	Engine, Actuators, and Limiters	33
6.	Effects of Atmospheric Turbulence	35
	Dryden Gust Spectrum Aerodynamic Models	
7.	Stability Augmentation Systems	38
8.	Structural-Mode Control Systems	43
9.	Flight Envelope of Validity – Trim Analysis	47
10.	References	50
	Appendix A – Users Manual	51

1. Introduction and Vehicle Description

The objective of this project was to develop a public domain, nonlinear aeroelastic simulation model (The Simulation) based on the Rockwell B-1 aircraft shown in Figure 1.1. This simulation model supports research being performed under the prime contract funded by the NASA Dryden Flight Research Center. Plus, The Simulation will be made available to the public to be used as a benchmark simulation for education and research on the dynamics of flexible aircraft and on aeroservoelastic-system identification and control. It is important to note that the simulation is not intended to model the actual B-1 aircraft, but rather a generic aircraft very similar to the B-1.

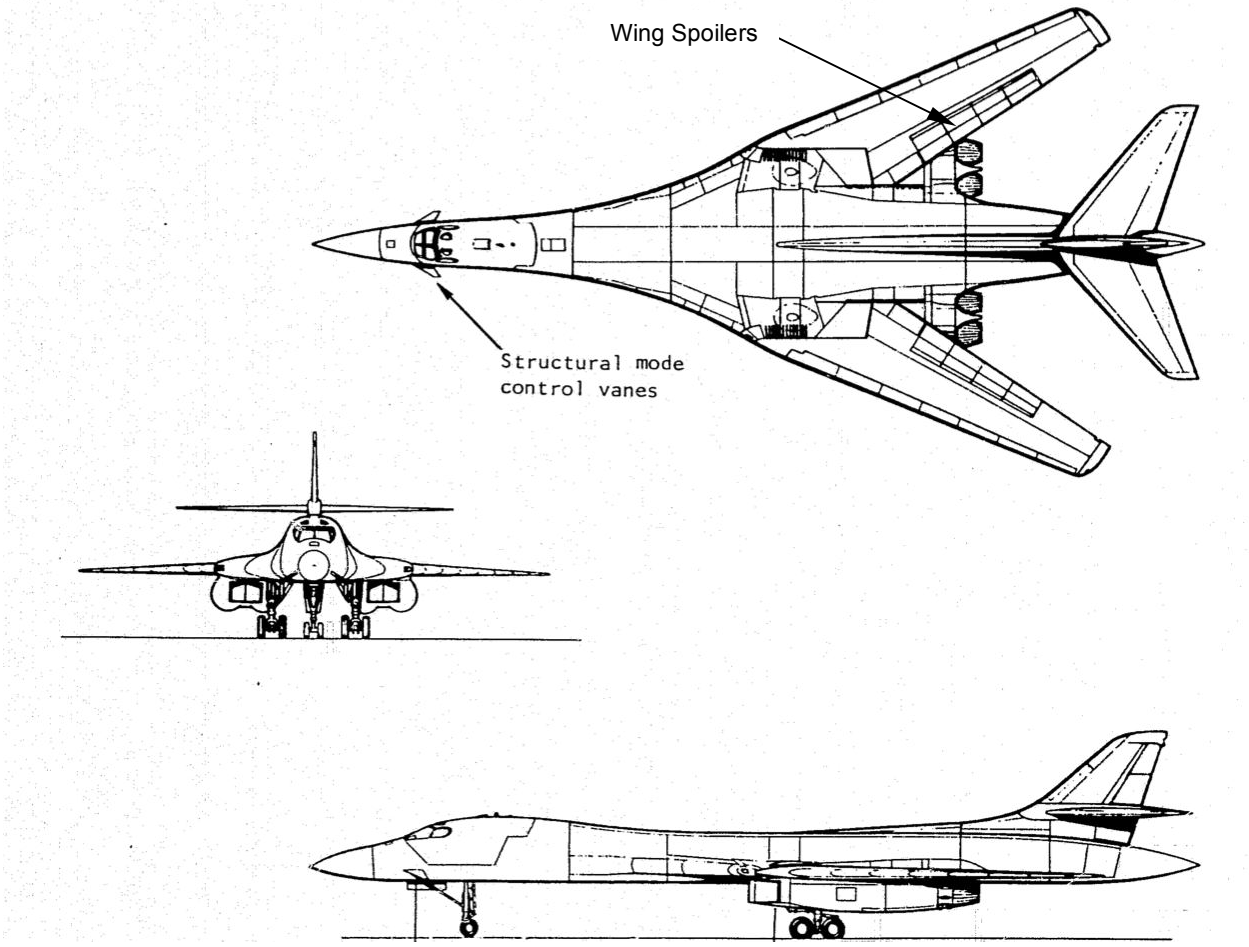

Figure, 1.1, The B-1 Aircraft

The B-1 has variable wing sweep, but we will only be considering the wing at a sweep angle of 65 degrees. Plus, we will assume the mass properties are fixed. The simulation includes models for several aerodynamic control surfaces used on the B-1 to affect control, including

Symmetric and anti-symmetric, all-movable horizontal tail

Wing upper-surface spoilers

Upper and lower split rudder

Structural-mode control vanes

Speed brakes are also used on the B-1, but are not included in this simulation. Additional relevant data further describing the B-1 are listed in Table 1.1.

Table 1.1, Characteristics of the B-1

Wing Geometry	$S = 1{,}950$ ft^2 $\bar{c} = 15.3$ ft $b = 136.7$ ft $\Lambda_{LE} = 65$ deg	*Inertias*	$I_{xx} = 9.5 \times 10^5$ sl-ft^2 $I_{yy} = 6.4 \times 10^6$ sl-ft^2 $I_{zz} = 7.1 \times 10^6$ sl-ft^2 $I_{xz} = -52{,}700$ sl-ft^2
Weight Mass	W = 288,000 lb $m = 8{,}944$ sl	*Vehicle length and c.g. location*	$L = 143$ ft. *c.g.* $= 0.25\ \bar{c}$ (FS 1061 in)

The fast-time simulation developed in this project is an extension of a real-time simulation developed and applied in an earlier study documented in [Waszak, Davidson, and Schmidt (1987)]. In this earlier study, a non-linear, piloted simulation of a vehicle similar to the B-1 was developed to investigate the effects of flexibility on aircraft handling qualities. Extending an existing, non-linear, real-time simulation of the B-1 available in the NASA Langley VMS simulation facility led to the simulation used in the 1987 study. The mathematical model of the original Langley simulation only included the rigid-body degrees of freedom while the model extensions in the 1987 study included the incorporation of two elastic degrees of freedom, or two aeroelastic modes. The modeling and simulation approach taken in the 1987 investigation is further documented in [Schmidt and Raney, (1998)].

The mathematical models used to develop The Simulation were, for the most part, available in the open literature. In particular, the primary sources of reference material and data for this project are the recent book by the author [Schmidt (2012)], and other publications by the author and colleagues [Waszak, Davidson, and Schmidt (1987)], plus [Waszak and Schmidt (1988)].

New model additions incorporated into The Simulation as part of the current project include the models for the dynamics and aerodynamic coupling associated with a second

antisymetric elastic mode, and the aerodynamic models for the forward control vanes. Neither of these components (additional vibration mode and vanes) was included in the mathematical models in the cited references, and hence required additional modeling as part of this project. In addition, the static pitch and roll stability of the vehicle, as modeled, were adjusted to extend the flight envelope of The Simulation. All these new models will be documented herein.

Additionally, stability-augmentations systems (SAS's) based on the B-1's are incorporated into The Simulation, and the B-1's systems are also described in the open literature. Specifically, SAS descriptions may be found in [Waszak, Davidson, and Schmidt (1987)], as well as in [Wykes, Byar, MacMiller, and Greek (1980)]. However, in the present project several enhancements have been incorporated into these SAS control laws, in order to better meet this program's objectives. And these enhancements will be documented herein as well.

The next extension included in The Simulation is the incorporation of structural-mode-control systems (SMCS), again based on those developed for the B-1. SMCS's were not included in the simulation model described in [Waszak, Davidson, and Schmidt (1987)]. But such feedback systems are fundamental to the objectives of this project. As with the SAS"s, the B-1 SMCS's are also described in the open literature. Specifically, these systems are documented in [Wykes, Borland, Klepl, and MacMiller (1977)] and [Wykes, Byar, MacMiller, and Greek (1980)]. In the present project, the control laws in the B-1 SMCS have been modified to improve their performance in The Simulation. These enhancements are also documented in this report.

The final extension incorporated into The Simulation is a model of the effects of atmospheric turbulence. Turbulence was also not considered in the 1987 study, and therefore no turbulence model is documented in [Waszak, Davidson, and Schmidt (1987)]. The models used in the current project are based on those presented in [Schmidt (2012)], and use the Dryden gust spectrum for the gust statistics.

The organization of this report parallels the structure of The Simulation, depicted in Figure 1.2. The blocks in the figure reflect the root-level blocks in The Simulation, and include

1. The equations of motion
2. The force and moment models
3. The measurements and responses
4. The engine, actuators, and limiters
5. The effects of atmospheric turbulence

6. The stability augmentation systems
7. The structural-mode control systems

The remaining sections of this report correspond to this list, plus a discussion of The Simulation's flight-envelope. Finally, a User's Guide is included in the Appendix.

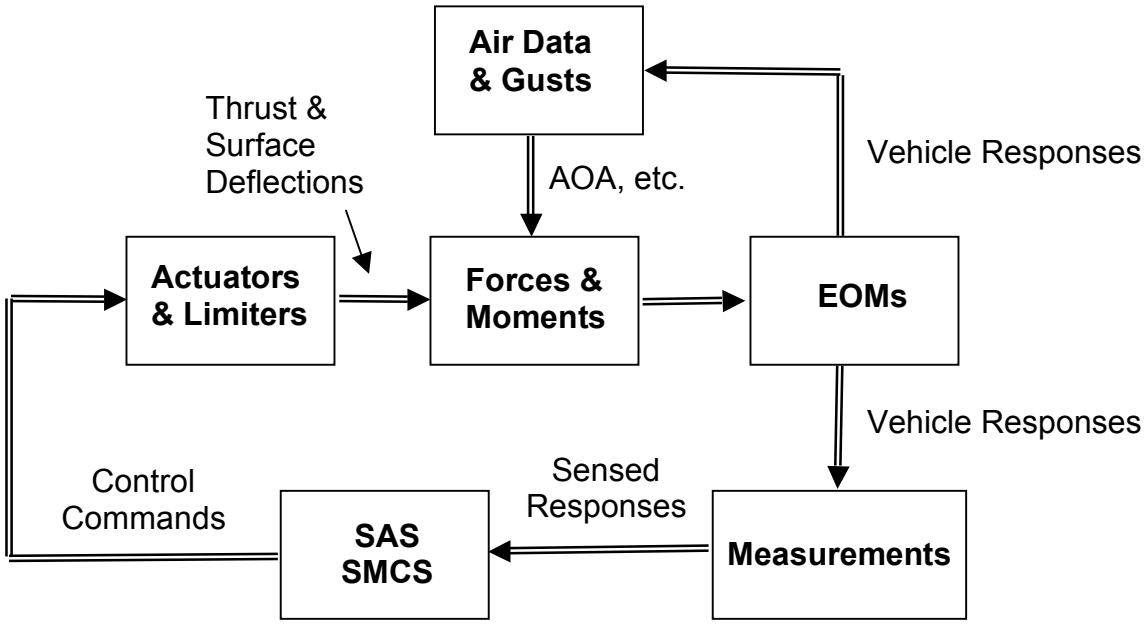

Figure 1.2, Block Diagram of The Simulation

2. Equations of Motion

Based on the development presented in [Schmidt (2012)], we define the relevant velocity, force, and moment vectors, and their components, given below.

$$
\begin{aligned}
&\text{Vehicle translational velocity vector} && \mathbf{V}_{\infty} = U\mathbf{i}_V + V\mathbf{j}_V + W\mathbf{k}_V \\
&\text{Vehicle rotational velocity vector} && \boldsymbol{\omega} = P\mathbf{i}_V + Q\mathbf{j}_V + R\mathbf{k}_V \\
&\text{Resultant aerodynamic force vector} && \mathbf{F}_{Aero} = F_{A_X}\mathbf{i}_V + F_{A_Y}\mathbf{j}_V + F_{A_Z}\mathbf{k}_V \\
&\text{Resultant propulsive force vector} && \mathbf{F}_{Prop} = F_{P_X}\mathbf{i}_V + F_{P_Y}\mathbf{j}_V + F_{P_Z}\mathbf{k}_V \\
&\text{Resultant aerodynamic moment vector} && \mathbf{M}_{Aero} = L_A\mathbf{i}_V + M_A\mathbf{j}_V + N_A\mathbf{k}_V \\
&\text{Resultant propulsive moment vector} && \mathbf{M}_{Prop} = L_P\mathbf{i}_V + M_P\mathbf{j}_V + N_P\mathbf{k}_V
\end{aligned}
\tag{2.1}
$$

These expressions define the components of the vectors (that is, *U, V, W*, etc.) in a vehicle-fixed coordinate system. For example, the vehicle's surge velocity U is the component of the vehicle's velocity vector in the $\mathbf{i}_V$ direction. But when dealing with flexible vehicles, this vehicle-fixed coordinate system must be carefully defined. And note that the vehicle's structure deforms relative to this coordinate frame.

As presented in the cited reference, if this coordinate system is selected such that the in-vacuo, free-vibration modes (or mode shapes) of the vehicle structure are orthogonal to the rigid-body mode shapes, and that the origin of this coordinate system is at the instantaneous center of mass (c.g.) of the vehicle, the equations of motion take on the particularly simple and attractive form used here. One vehicle-fixed coordinate frame that satisfies this condition is the structural reference frame used in the definition of the free-vibration mode shapes. Therefore, we have adopted this structural-referenced coordinate frame as the vehicle-fixed axis used in this project.

In addition to the quantities defined in Eqns. (2.1), the usual Euler angles are also employed to define the orientation of the vehicle-fixed coordinate frame with respect to the inertial (taken to be Earth fixed). These angles are the

Heading angle, ψ
Pitch-attitude angle, θ
Roll angle, ϕ

As a result of these definitions and assumptions, and letting the vehicle's mass be denoted as m, the equations of motion governing the six rigid-body degrees of freedom are given

in Eqns. 2.2. Here, the vehicle is assumed symmetric with respect to its XZ plane, and the moments and products of inertia are as typically defined in Table 2.1. Due to elastic deformation the inertias are not strictly constant. But here the usual assumption is made that these deformations are sufficiently small such that the mass and inertias may be taken as constant. In this study, the weight is taken to be 288,000 lb, and the inertias are listed in Table 2.2.

$$
\begin{aligned}
m\left(\dot{U} + QW - VR\right) &= -mg\sin\theta + F_{A_X} + F_{P_X} \\
m\left(\dot{V} + RU - PW\right) &= mg\cos\theta\sin\phi + F_{A_Y} + F_{P_Y} \\
m\left(\dot{W} + PV - QU\right) &= mg\cos\theta\cos\phi + F_{A_Z} + F_{P_Z} \\
I_{xx}\dot{P} - I_{xz}\left(\dot{R} + PQ\right) + \left(I_{zz} - I_{yy}\right)RQ &= L_A + L_P \\
I_{yy}\dot{Q} + \left(I_{xx} - I_{zz}\right)PR + I_{xz}\left(P^2 - R^2\right) &= M_A + M_P \\
I_{zz}\dot{R} - I_{xz}\left(\dot{P} - QR\right) + \left(I_{yy} - I_{xx}\right)PQ &= N_A + N_P
\end{aligned}
\tag{2.2}
$$

Table 2.1, Definitions of Moments and Products of Inertia

$I_{xx} = \int_{Vol}\left(y^2 + z^2\right)\rho_V dV$	$I_{xy} = I_{yx} = \int_{Vol} xy\rho_V dV$
$I_{yy} = \int_{Vol}\left(x^2 + z^2\right)\rho_V dV$	$I_{xz} = I_{zx} = \int_{Vol} xz\rho_V dV$
$I_{zz} = \int_{Vol}\left(x^2 + y^2\right)\rho_V dV$	$I_{yz} = I_{zy} = \int_{Vol} yz\rho_V dV$

Table 2.2, Inertias (constant)

I_{xx} = 9.5x10^5 sl-ft^2	I_{xy} = 0
I_{yy} = 6.4x10^6 sl-ft^2	I_{xz} = -52,700 sl-ft^2
I_{xx} = 7.1x10^6 sl-ft^2	I_{yz} = 0

In addition to the six equations of motion given above, we also have the kinematic equations governing the three Euler angles, plus an additional kinematic equation governing altitude *h*. These additional equations are given in Eqns. 2.3.

$$\begin{aligned}
\dot{\phi} &= P + Q\sin\phi\tan\theta + R\cos\phi\tan\theta \\
\dot{\theta} &= Q\cos\phi - R\sin\phi \\
\dot{\psi} &= \left(Q\sin\phi + R\cos\phi\right)\sec\theta \\
\dot{h} &= U\sin\theta - V\sin\phi\cos\theta - W\cos\phi\cos\theta
\end{aligned} \tag{2.3}$$

Now let the generalized coordinate associated with the *i*'th free-vibration mode of the vehicle's structure be defined as η_i, the in-vacuo vibration frequency of that mode as ω_i, and the in-vacuo damping of the mode as ζ_i. In addition, let the generalized mass of that vibration mode be $\mathcal{M}_i$, and the generalized force acting on that degree of freedom due to aerodynamic and propulsive forces be Q_i. Then the equations of motion governing the elastic degrees of freedom of the vehicle, as shown in [Schmidt (2012)], are as given in Eqn. 2.4. In this equation, *n* is the total number of elastic degrees of freedom included in the model, where each vibration mode constitutes a degree of freedom of the system.

$$\ddot{\eta}_i + 2\zeta_i\omega_i\dot{\eta}_i + \omega_i^2\eta_i = \frac{Q_i}{\mathcal{M}_i},\ i = 1\ldots n \tag{2.4}$$

The vibration modes selected to be included in this model are the three lowest-frequency symmetric vibration modes (modes 1-3 in The Simulation) and the two lowest-frequency anti-symmetric vibration modes (modes 4-5 in The Simulation). The selection of these vibration modes is justified based not only on their modal frequencies and mode shapes, but also their generalized masses. Due to limited bandwidth actuators and the bandwidth of the SAS's, the elastic modes most likely to interact with the rigid-body degrees of freedom and the feedback systems are those with the lowest frequencies ω_i. But from Eqn. 2.4, also note that modes with large generalized masses $\mathcal{M}_i$ will be difficult to excite.

The frequencies and generalized masses of the first four (lowest frequencies) symmetric and anti-symmetric vibration modes for the B-1 vehicle, taken from [Freeman and Rozsa (1971)], are listed in Table 2.3. Note the significant differences between the generalized masses, due to the normalization technique used in the reference for the vibration mode shapes. Based on these considerations (along with the mode shapes discussed below), the modes expected to be the most significant in terms of flexible-rigid dynamic interactions and cockpit ride quality are those marked with an asterisk. And these are the modes selected for inclusion in The Simulation.

Table 2.3, Vibration Modal Frequencies and Generalized Masses

Symmetric Modes		**Anti-Symmetric Modes**	
Frequency, r/s	Generalized Mass, sl-ft^2	Frequency, r/s	Generalized Mass, sl-ft^2
12.6*	184*	12.9*	28,991*
14.1*	9,587*	16.5*	136*
21.2*	1,334*	20.2	26,874
22.1	436,000	22.1	74,062

As noted, the vibration mode shapes were also considered in the mode-selection process. The plunge-displacement v_Z modes shapes for the first four symmetric modes are sketched in Fig. 2.1. The data plotted are the plunge displacements for each mode shape along the fuselage centerline, and along the quarter chords of the wing and horizontal tail. The wing and tail twist is not plotted for simplicity. All these modes have been normalized to unity displacement at the nose, which leads to the vastly differing generalized masses.

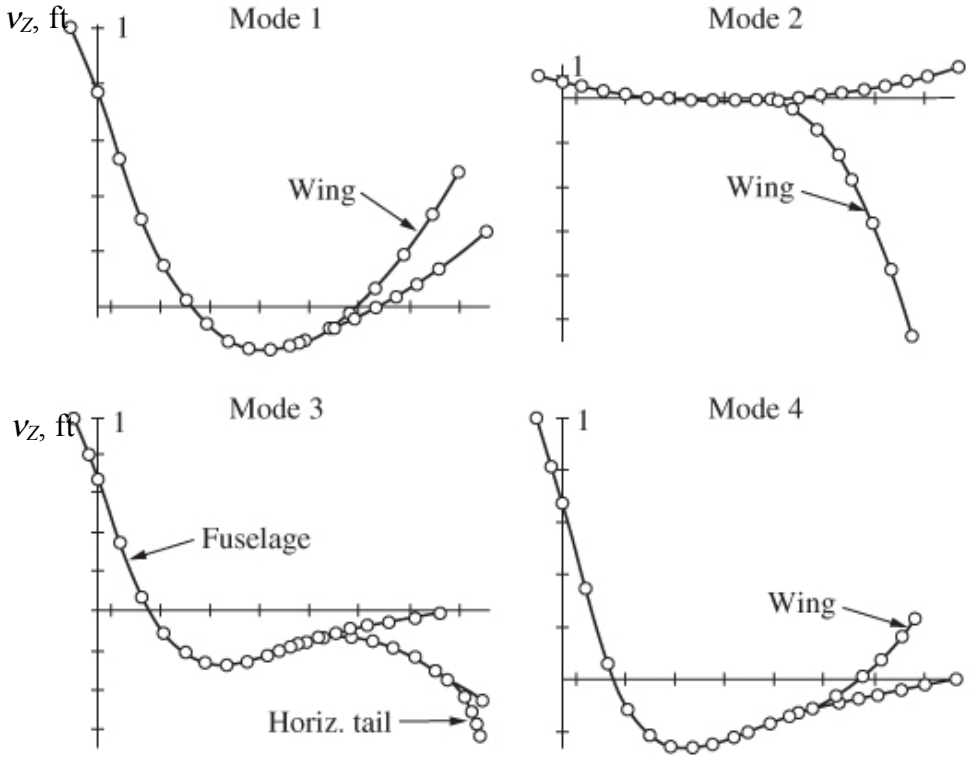

Figure 2.1, Mode Shapes – First Four Symmetric Vibration Modes

Note that the first, third, and fourth mode in this figure exhibit significant modal displacement near the nose, where the cockpit and control vanes are located, while the second

mode is essentially a wing-bending mode. This wing mode may produce lift and pitching moment, if excited, but most of the motion will be wing, rather than cockpit, deformation.

Figure 2.2 shows the plunge- v_Z and lateral- v_Y displacement mode shape for the first anti-symmetric mode. (The plot quality is poor, due to the poor quality of the original.). This mode is also primarily an wing-bending mode, analogous to Mode 2 above. And so the remarks made with reference to the previous mode also apply here. However, the second anti-symmetric mode is a lateral fuselage-bending mode, analogous to Mode 1 above. The lateral- v_Y displacement mode shape showing only the fuselage and vertical tail is plotted in Fig. 2.3. The plunge displacements of the wing and horizontal tail are quite small, and are not plotted.

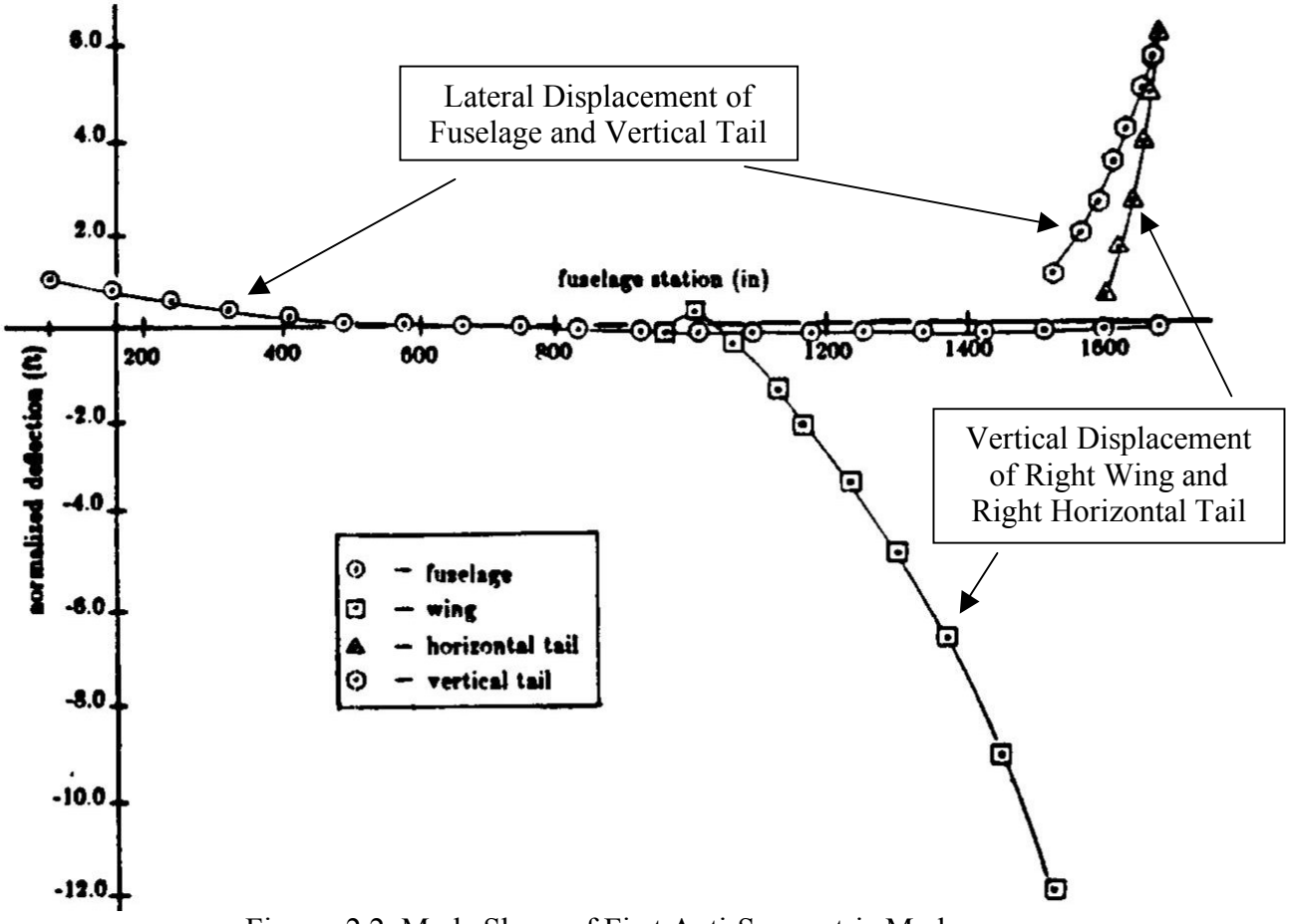

Figure, 2.2, Mode Shape of First Anti-Symmetric Mode

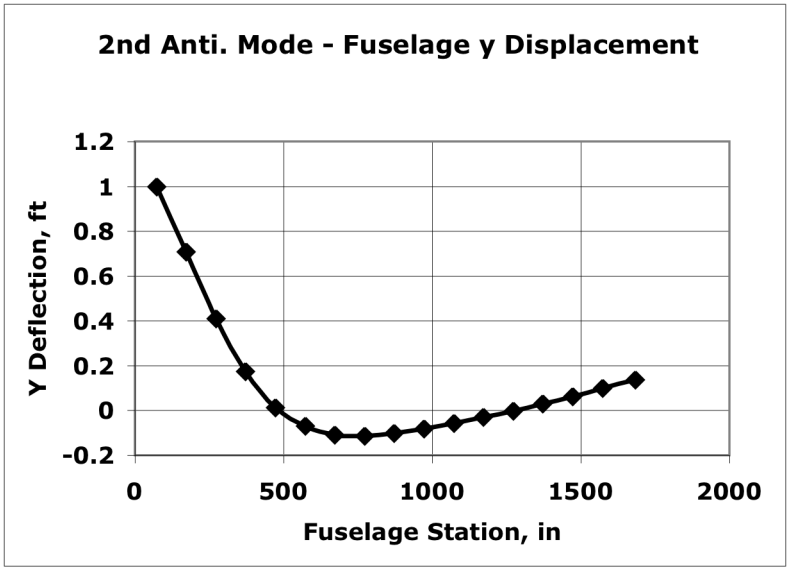

Figure, 2.3, Fuselage/Vertical Tail Lateral Displacement, Second Anti-Symmetric Mode

Based on this analysis and the simulation results evaluated, the first symmetric (Mode 1 in The Simulation) and second anti-symmetric (Mode 5 in The Simulation) are clearly the most significant, with regards to the level of excitation and the contribution to cockpit accelerations.

In summary, the 15 equations of motion used in The Simulation are those given in Eqns 2.2, 2.3, and. 2.4. And the number of elastic degrees of freedom included, or *n*, is five (3+2).

3. Force and Moment Models

The forces and moments appearing in the equations of motion arise from propulsive and aerodynamic effects. The models for these forces and moments are primarily taken from in [Waszak, Davidson, and Schmidt (1987)] and [Schmidt (2012)], except for the models developed as part of this project.

Dealing with the aerodynamic forces and moments first, these depend on the aerodynamic angles of attack α and sideslip β, where in the absence of gusts

$$\begin{aligned} \alpha &= \tan^{-1}\left(\frac{W}{U}\right) & \dot{\alpha} &= \frac{U\dot{W} - W\dot{U}}{U^2 + W^2} \\ \beta &= \sin^{-1}\left(\frac{V}{V_\infty}\right) & \dot{\beta} &= \frac{V_\infty \dot{V} - V\dot{V}_\infty}{V_\infty^2 \cos\beta} \\ V_\infty &= \sqrt{\left(U^2 + V^2 + W^2\right)} & \dot{V}_\infty &= \left(U\dot{U} + V\dot{V} + W\dot{W}\right)/V_\infty \end{aligned} \tag{3.1}$$

Additionally, the forces and moments depend on the deflections of the aerodynamic control surfaces. For the vehicle in question, shown in Fig. 3.1, these control-surface deflections are

Symmetric horizontal tail, δ_H

Differential horizontal tail, δ_{DH} (+ yielding positive rolling moment)

Wing upper-surface spoiler, δ_{sp} (deflect on either left or right wing)

Upper rudder surface, δ_{RU}

Lower rudder surface, δ_{RL}

The force and moment equations used in The Simulation are functions of aerodynamic coefficients, to be discussed below, plus dynamic pressure q_∞, wing planform area S, wing mean aerodynamic chord $\bar{c}$, and wing span b. For the vehicle in question these parameters are given as

$$\begin{aligned} S &= 1950 \text{ ft}^2 \\ \bar{c} &= 15.3 \text{ ft} \\ b &= 136.7 \text{ ft} \end{aligned} \tag{3.2}$$

while the dynamic pressure is $q_\infty = \frac{1}{2}\rho V_\infty^2$.

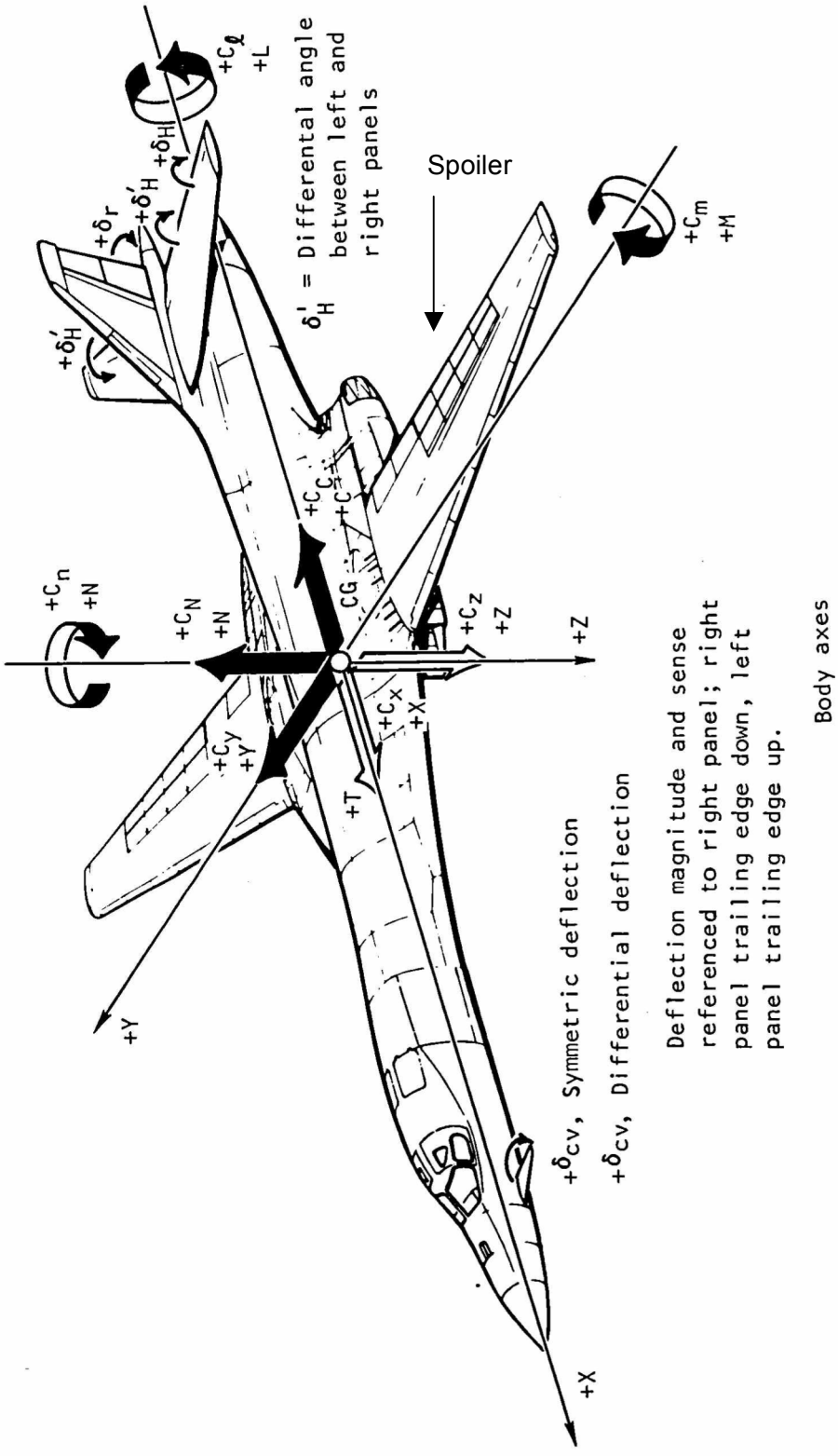

Figure, 3.1, The B-1 Vehicle (Wings Forward), With Sign Conventions

The atmospheric density ρ, as well as the sonic velocity V_{sonic}, are available from an atmospheric model, in The Simulation, based on the ARDC Standard Atmosphere. See [Schmidt (2012)].

Consistent with [Schmidt (2012)], the components of the resultant aerodynamic force and moment vectors acting on the vehicle are given in coefficient form in Eqns. (3.3a and b). In this study, and consistent with the study reported in [Waszak, Davidson, and Schmidt (1987)], the effects of unsteady aerodynamics are assumed small, and are neglected. This assumption is based on the fact that only the lowest-frequency vibration modes are included in the model, so the reduced frequencies will be small. Unsteady effects become significant at higher reduced frequencies.

$$
\begin{aligned}
F_{A_X} &= q_\infty S\left(C_{X_0} + C_{X_Q} Q + C_{X_{\delta H}} \delta_H + C_{X_{\delta sp}} \delta_{sp}\right) \\
F_{A_Y} &= q_\infty S\left(\begin{array}{l} C_{Y_\beta}\beta + C_{Y_{\delta DH}}\delta_{DH} + C_{Y_{\delta sp}}\delta_{sp} + C_{Y_{\delta RU}}\delta_{RU} \\ +C_{Y_{\delta RL}}\delta_{RL} + C_{Y_{\delta cvanti}}\delta_{cvanti} + \sum_{i=4}^{5}\left(C_{Y_{\eta_i}}\eta_i + \frac{1}{V_\infty}C_{Y_{\dot\eta_i}}\dot\eta_i\right)\end{array}\right) \\
F_{A_Z} &= q_\infty S\left(\begin{array}{l} C_{Z_0} + \frac{1}{V_\infty}C_{Z_Q}Q + C_{Z_{\delta H}}\delta_H + C_{Z_{\delta sp}}\delta_{sp} \\ +C_{Z_{\delta cvsym}}\delta_{cvsym} + \sum_{i=1}^{3}\left(C_{Z_{\eta_i}}\eta_i + \frac{1}{V_\infty}C_{Z_{\dot\eta_i}}\dot\eta_i\right)\end{array}\right)
\end{aligned}
\tag{3.3a}
$$

$$
\begin{aligned}
L_A &= q_\infty Sb\left(\begin{array}{l} C_{L_\beta}\beta + \frac{1}{V_\infty}\left(C_{L_P}P + C_{L_R}R\right) + C_{L_{\delta DH}}\delta_{DH} + C_{L_{\delta sp}}\delta_{sp} \\ +C_{L_{\delta RU}}\delta_{RU} + C_{L_{\delta RL}}\delta_{RL} + \sum_{i=4}^{5}\left(C_{L_{\eta_i}}\eta_i + \frac{1}{V_\infty}C_{L_{\dot\eta_i}}\dot\eta_i\right)\end{array}\right) \\
M_A &= q_\infty S\overline{c}\left(\begin{array}{l} C_{M_0} + \frac{1}{V_\infty}\left(C_{M_Q}Q + C_{M_\alpha}\dot\alpha\right) + C_{M_{\delta H}}\delta_H + C_{M_{\delta sp}}\delta_{sp} \\ +C_{M_{\delta cvsym}}\delta_{cvsym} + \sum_{i=1}^{3}\left(C_{M_{\eta_i}}\eta_i + \frac{1}{V_\infty}C_{M_{\dot\eta_i}}\dot\eta_i\right)\end{array}\right) \\
N_A &= q_\infty Sb\left(\begin{array}{l} C_{N_\beta}\beta + \frac{1}{V_\infty}\left(C_{N_{\dot\beta}}\dot\beta + C_{N_P}P + C_{N_R}R\right) + C_{N_{\delta DH}}\delta_{DH} + C_{N_{\delta sp}}\delta_{sp} \\ +C_{N_{\delta RU}}\delta_{RU} + C_{N_{\delta RL}}\delta_{RL} + C_{N_{\delta cvanti}}\delta_{cvanti} + \sum_{i=4}^{5}\left(C_{N_{\eta_i}}\eta_i + \frac{1}{V_\infty}C_{N_{\dot\eta_i}}\dot\eta_i\right)\end{array}\right)
\end{aligned}
\tag{3.3b}
$$

Many of the coefficients in these equations are non-linear functions of vehicle angle of attack, and the numerical values of most coefficients have been previously published elsewhere,

notably [Schmidt (2012)] and [Waszak, Davidson, and Schmidt (1987)]. Consequently, they will not all be tabulated again here. Specifically, the coefficients used in the model for the 1987 study are listed in Volume 2, Tables A.1 and A.2, Pages 2-4 of the reference. Plus the aeroelastic coefficients $C_{\bullet_{\eta_i}}$ and $C_{\bullet_{\dot{\eta}_i}}$ for i = 1-3 (the three symmetric modes) are presented in [Schmidt (2012)], and for i = 4 (the first anti-symmetric mode) in [Waszak, Davidson, and Schmidt (1987)].

But some new aeroelastic coefficients have been derived in this study, plus two important aerodynamic moment coefficients in the models for the vehicle pitching and rolling moment now differ from those listed in [Waszak, Davidson, and Schmidt (1987)]. First, the coefficients $C_{\bullet_{\eta_5}}$ and $C_{\bullet_{\dot{\eta}_5}}$ associated with the newly added elastic mode, the second anti-symmetric mode, were derived in this study using the approach presented in [Schmidt (2012)]. For completeness, values for all the aeroelastic coefficients $C_{\bullet_{\eta_i}}$ and $C_{\bullet_{\dot{\eta}_i}}$ appearing in Eqns. (3.2) are summarized in Table 3.1.

Table 3.1, Aeroelastic Coefficients in Eqns. (3.2a and b)

Coefficient	**Value, /rad**	**Coefficient**	**Value, /rad**
$C_{Y_{\eta_4}}$	-0.009	$C_{Y_{\dot{\eta}_4}}$	-1.128
$C_{Y_{\eta_5}}$	-0.005	$C_{Y_{\dot{\eta}_5}}$	-0.067
$C_{Z_{\eta_1}}$	-0.029	$C_{Z_{\dot{\eta}_1}}$	-0.658
$C_{Z_{\eta_2}}$	0.306	$C_{Z_{\dot{\eta}_2}}$	7.896
$C_{Z_{\eta_3}}$	0.015	$C_{Z_{\dot{\eta}_3}}$	0.461
$C_{M_{\eta_1}}$	-0.032	$C_{M_{\dot{\eta}_1}}$	-1.184
$C_{M_{\eta_2}}$	-0.025	$C_{M_{\dot{\eta}_2}}$	9.409
$C_{M_{\eta_3}}$	0.041	$C_{M_{\dot{\eta}_3}}$	1.316
$C_{L_{\eta_4}}$	0.068	$C_{L_{\dot{\eta}_4}}$	1.661
$C_{L_{\eta_5}}$	-0.001	$C_{L_{\dot{\eta}_5}}$	-0.013
$C_{N_{\eta_4}}$	0.008	$C_{N_{\dot{\eta}_4}}$	0.355
$C_{N_{\eta_5}}$	0.001	$C_{N_{\dot{\eta}_5}}$	0.021

In addition, the static pitch stability of the vehicle was adjusted to extend the flight envelope. The first adjustment was to the pitching-moment coefficient (all deflections = 0) at angles of attack above five degrees, as shown in Fig. 3.2. The adjusted data extends the range of angle of attack over which the vehicle is statically stable in pitch to 10 degrees, instead of the original five degrees. Also, the static roll stability of the vehicle was adjusted, as shown in Fig. 3.3. This data adjustment reduces the level of roll instability at negative angles of attack.

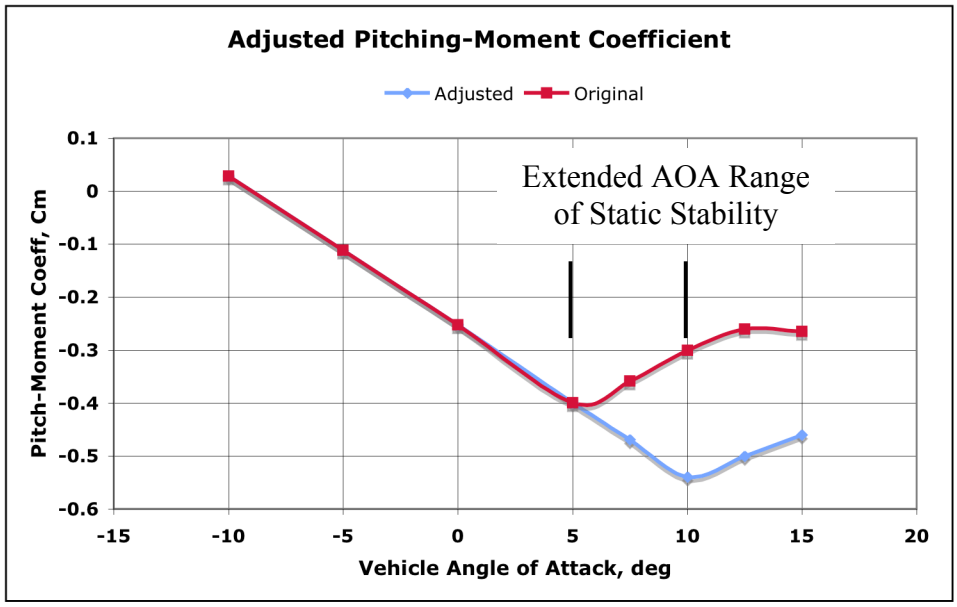

Figure 3.2, Adjusted Pitch Stability, C_{m_α}

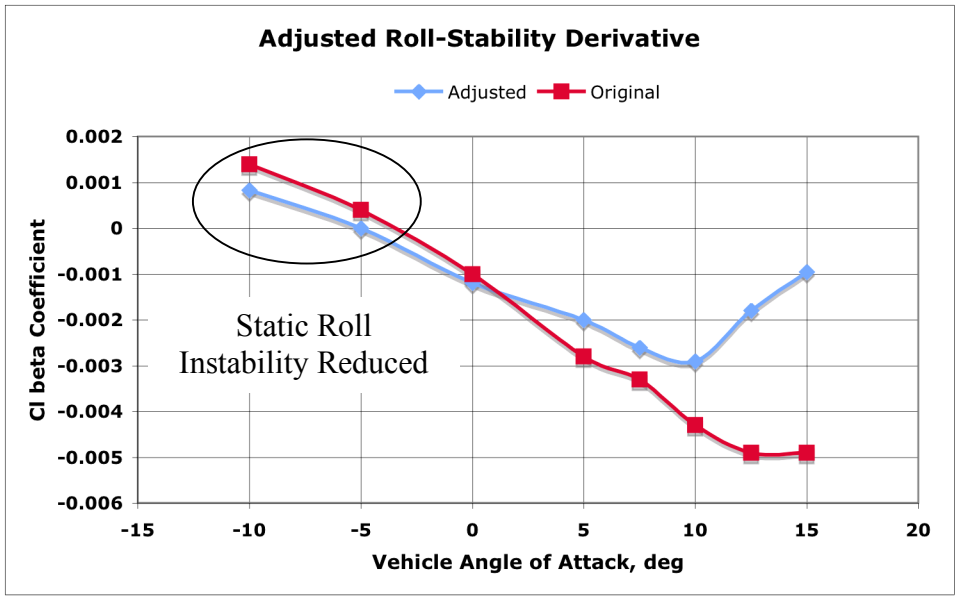

Figure 3.3, Adjusted Roll-Stability, C_{l_β}

Finally, since the forward control vanes are new additions to the simulation developed here, the aerodynamic model for these vanes was also derived. A slightly simplified model was developed based on the data in [Wykes, Borland, Klepl, and MacMiller (1977)], shown in Figs. 3.4, 3.5, and 3.6. These wind-tunnel data were obtained at M = 0.85, but are assumed here to be independent of Mach number.

Figure 3.4 presents the normal force coefficient C_N (= $-C_Z$) for symmetric vane deflections, as a function of local vane angle of attack α_V. This local angle of attack is defined as

$$\alpha_V = \alpha \cos\Gamma + \delta_{cvsym} - \varepsilon \tag{3.4}$$

where α = vehicle angle of attack

Γ = vane dihedral angle = -30 deg

δ_{cvsym} = symmetric vane deflection (+ trailing-edge down)

ε = local angle of downwash

The local downwash angle ε is a function of vehicle angle of attack α, as shown in Fig. 3.5. (This data is shown for two different vane geometries, but the results are essentially the same.)

These two data sets given in Figs. 3.4 and 3.5 were directly implemented into The Simulation to model $C_{Z_{\delta_{cvsym}}}$, using straight-line fits to the data in Figs. 3.4 and 3.5, along with appropriate vane-deflection limits. The pitching moment, or $C_{M_{\delta_{cvsym}}}$, due to symmetric vane deflection was easily obtained knowing the moment arm, or the distance between the c.g. (Fuselage Station 1061 in) and the control-vane (Fuselage Station 225 in).

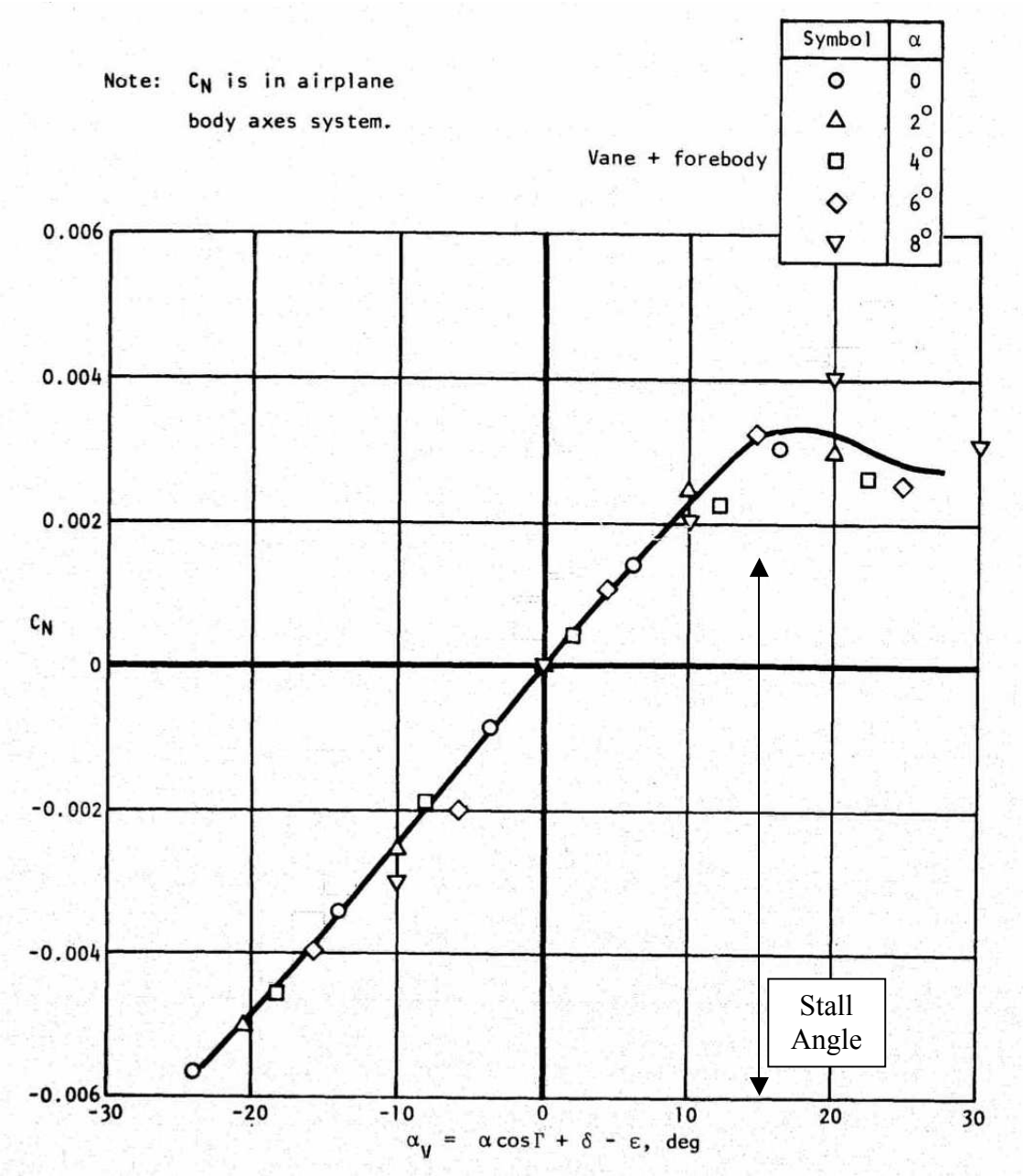

Figure 3.4, Normal-Force Coefficient for Symmetric Vane Deflections

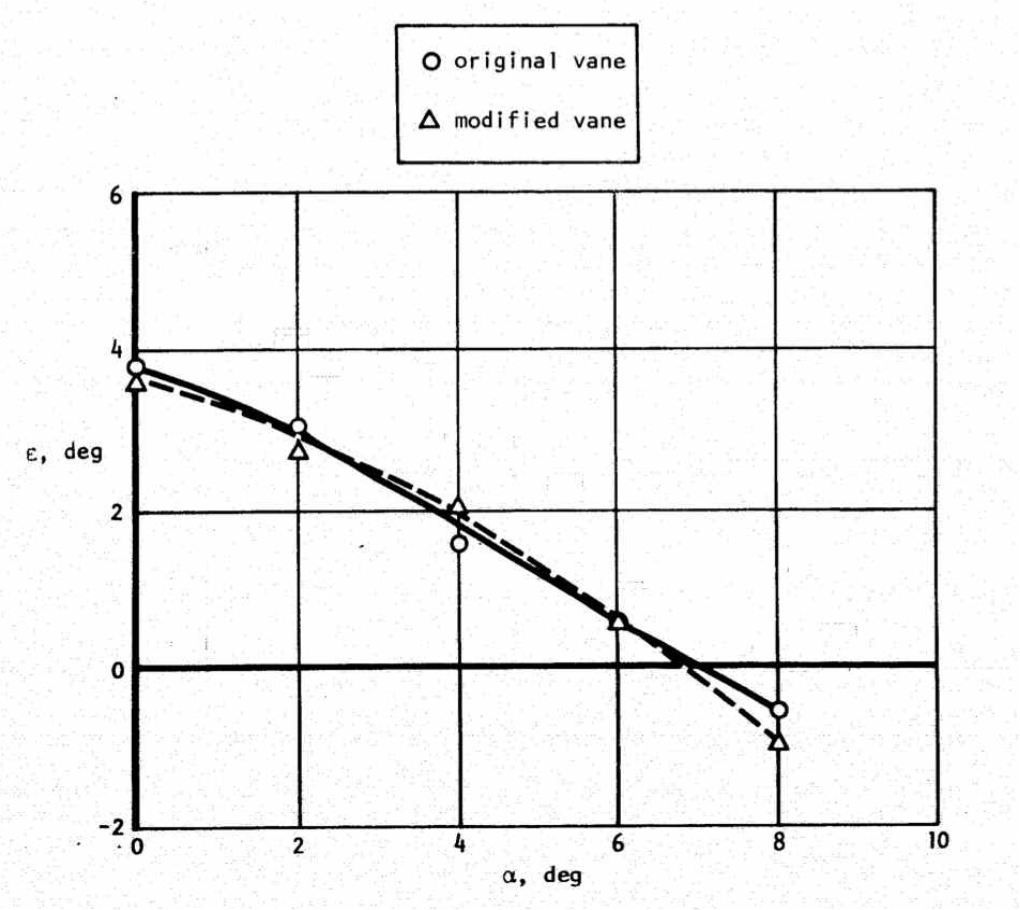

Figure 3.5, Local Downwash Angle at the Vanes

The side force (coefficient) due to anti-symmetric vane deflection $C_{Y_{\delta_{cvanti}}}$ is given in Fig. 3.6. These results were incorporated into The Simulation as a function of δ_{cvanti} and α by using straight-line fits to the data, along with appropriate vane-deflection limits. The yawing moment, or $C_{N_{\delta_{cvanti}}}$, due to anti-symmetric vane deflection was easily obtained knowing the moment arm, or the distance between the c.g. (FS 1061) and the control-vane (FS 225) fuselage stations.

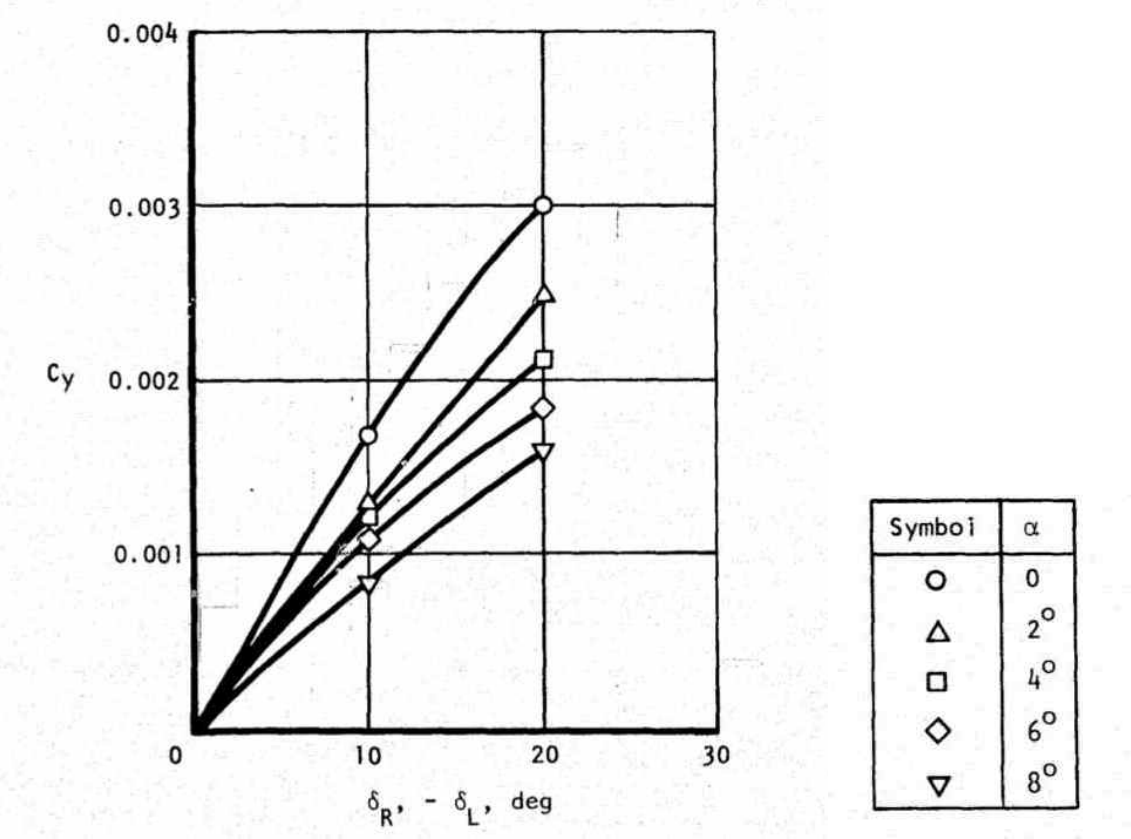

Figure 3.6, Side Force Coefficient Due to Anti-Symmetric Vane Deflections

The models for the generalized forces Q_1 – Q_5 appearing in Eqns. 2.4 may also be expressed in coefficient form, and these are given in Eqns. 3.5. The numerical values for all these coefficients, except for those corresponding to $i = 5$, are also published in [Schmidt (2012)] and

$$Q_i = q_\infty S\overline{c}\left(\begin{array}{l} C_{Q_{i_\alpha}}\alpha + \dfrac{1}{V_\infty}C_{Q_{i_Q}}Q + C_{Q_{i_H}}\delta_H + C_{Q_{i_{|sp|}}}\left|\delta_{sp}\right| \\ +C_{Q_{i_{cvsym}}}\delta_{cvsym} + \displaystyle\sum_{j=1}^{3}\left(C_{Q_{i_{\eta_j}}}\eta_j + \frac{1}{V_\infty}C_{Q_{i_{\dot\eta_j}}}\dot\eta_j\right) \end{array}\right),\ i = 1...3$$

$$Q_i = q_\infty S\overline{c}\left(\begin{array}{l} C_{Q_{i_\beta}}\beta + \dfrac{1}{V_\infty}\left(C_{Q_{i_P}}P + C_{Q_{i_R}}R\right) + C_{Q_{i_{DH}}}\delta_{DH} + C_{Q_{i_{sp}}}\delta_{sp} + C_{Q_{i_{RU}}}\delta_{RU} \\ +C_{Q_{i_{RL}}}\delta_{RL} + C_{Q_{i_{cvanti}}}\delta_{cvanti} + \displaystyle\sum_{j=4}^{5}\left(C_{Q_{i_{\eta_j}}}\eta_j + \frac{1}{V_\infty}C_{Q_{i_{\dot\eta_j}}}\dot\eta_j\right) \end{array}\right),\ i = 4,5$$

(3.5)

[Waszak, Davidson, and Schmidt (1987)]. But those associated with the newly added vibration mode, Mode 5, were derived in this study. For completeness, all the coefficients appearing in Eqns. (3.5), with he exception of $C_{Q_{i_{cvsym}}}$ and $C_{Q_{i_{cvanti}}}$, are listed in Tables 3.2 and 3.3.

Table 3.2, Aeroelastic Coefficients For the Symmetric Modes

Coefficient	**Value, /rad** $i = 1$	**Value, /rad** $i = 2$	**Value, /rad** $i = 3$
$C_{Q_{i_\alpha}}$	-0.0149	0.0258	0.0149
$C_{Q_{i_Q}}$	-0.726	0.089	0.304
$C_{Q_{i_H}}$	-0.0128	-0.0642	0.0256
$C_{Q_{i_{sp}}}$	8.418E-4	-6.817E-2	-1.885E-3
$C_{Q_{i_{cvsym}}}$	(See Text)		
$C_{Q_{i_{\eta_1}}}$	5.85E-5	4.21E-3	2.91E-4
$C_{Q_{i_{\eta_2}}}$	-9.0E-5	-9.22E-2	1.44E-3
$C_{Q_{i_{\eta_3}}}$	3.55E-4	1.97E-3	-3.46E-4
$C_{Q_{i_{\dot{\eta}_1}}}$	-0.0032	0.0665	-0.0048
$C_{Q_{i_{\dot{\eta}_2}}}$	-0.0015	-2.277	0.1494
$C_{Q_{i_{\dot{\eta}_3}}}$	0.0050	0.0320	-0.0001

Knowing the vertical and lateral forces produced by the vanes, or $C_{Z_{\delta_{cvsym}}}$ and $C_{Y_{\delta_{cvanti}}}$, allows for the determination of the generalized-force coefficients $C_{Q_{i_{cvsym}}}$ and $C_{Q_{i_{cvanti}}}$ in Tables in 3.2 and 3.3. These latter coefficients are also functions of the *Z* or *Y* displacements at the vanes associated with the symmetric or anti-symmetric vibration modes, respectively. For Modes 1-3 the *Z* mode-shape displacements are 0.58, 0.58, and 0.4 ft., and for Modes 4 and 5, the *Y* mode-shape displacements are 0.65 and 0.55 ft. Finally, since $C_{Z_{\delta_{cvsym}}}$ and $C_{Y_{\delta_{cvanti}}}$ are functions of vehicle angle of attack and vane deflection, $C_{Q_{i_{cvsym}}}$ and $C_{Q_{i_{cvanti}}}$ are also functions of these variables.

Table 3.3, Aeroelastic Coefficients For the Anti-Symmetric Modes

Coefficient	**Value, /rad** $i = 4$	**Value, /rad** $i = 5$
$C_{Q_{i_\beta}}$	-0.0017	-0.0044
$C_{Q_{i_P}}$	0.0070	-0.1170
$C_{Q_{i_R}}$	0.0034	0.1835
$C_{Q_{i_{DH}}}$	-0.0240	0.0062
$C_{Q_{i_{sp}}}$	0.0820	0.0002
$C_{Q_{i_{RU}}}$	0.0137	0.0023
$C_{Q_{i_{RL}}}$	0.0041	0.0010
$C_{Q_{i_{cvanti}}}$	(See Text)	
$C_{Q_{i_{\eta_4}}}$	-0.1118	0.0004
$C_{Q_{i_{\eta_5}}}$	0.0008	0
$C_{Q_{i_{\dot{\eta}_4}}}$	-4.123	0.0046
$C_{Q_{i_{\dot{\eta}_5}}}$	0.0038	-0.0006

The final topic to be discussed in this section involves the forces and moments associated with propulsive effects appearing in the equations in Eqns. 2.2. But these forces and moments are much simpler to address than the aerodynamic models. Knowing the propulsive thrust from the engine model, and assuming the thrust acts along the vehicle's fuselage-referenced *X* axis, the axial-force component $F_{P_X} = thrust$, while the other two force components F_{P_Y} and F_{P_Z} are zero. Likewise, assuming the line of action of the thrust vector acts through the c.g, or the thrust-cg offset is zero, the three components of propulsive moment L_P, M_P, and N_P are all zero.

The propulsive effects on the generalized forces appearing in Eqns. 2.4 are all assumed to be negligible. This is justified by the fact that the propulsive force, acting along the vehicle's *X* axis, would only significantly contribute to a modal generalized force if that mode shape contained significant deformation along the *X* axis, rather than *Y* or *Z*. And since the structure is quite stiff in this direction, modal deformations in this direction are very small.

4. Measurement Set – Vehicle's Responses

Important vehicle responses include the following:

- Vehicle velocity, V_∞
- Vehicle angles of attack and sideslip, α and β
- Flight-path angle, γ
- Sensed angular rates at the vehicle c.g., P_{cg}, Q_{cg}, and R_{cg}
- Sensed accelerations at the vehicle c.g., $n_{Y\,cg}$, $n_{Z\,cg}$
- Sensed accelerations at the cockpit/control-vane location, $n_{Y\,cp}$, $n_{Z\,cp}$

Models for all vehicle responses are taken from [Waszak, Davidson, and Schmidt (1987)] and [Schmidt (2012)].

The vehicle velocity and angles of attack and sideslip were given in Eqns. 3.1, but are repeated here for convenience.

$$\begin{aligned} \mathbf{V}_\infty &= U\mathbf{i}_V + V\mathbf{j}_V + W\mathbf{k}_V \\ V_\infty &= \sqrt{\left(U^2 + V^2 + W^2\right)} \\ \alpha &= \tan^{-1}\left(\frac{W}{U}\right) \\ \beta &= \sin^{-1}\left(\frac{V}{V_\infty}\right) \end{aligned} \tag{4.1}$$

These expressions are valid in the absence of winds, but are modified when wind gusts are included. These modifications will be discussed in Section 6, when the turbulence models are presented.

Two example step responses obtained from The Simulation, starting from an initial level, trim flight condition of Mach = 0.6 and altitude h = 5000 ft (no SAS or SMCS), are shown in Figs. 4.1 and 4.2. The first figure is the angle-of-attack response to a negative-one-degree commanded symmetric-horizontal-tail deflection (actuator input), while the second is the response to a one-degree commanded roll-command doublet (actuator input). The roll-command input is a blend of commanded spoiler and differential tail deflections, as discussed in Section 7. In the doublet, the command reverses at 5 seconds, and then returns to zero at 10 seconds

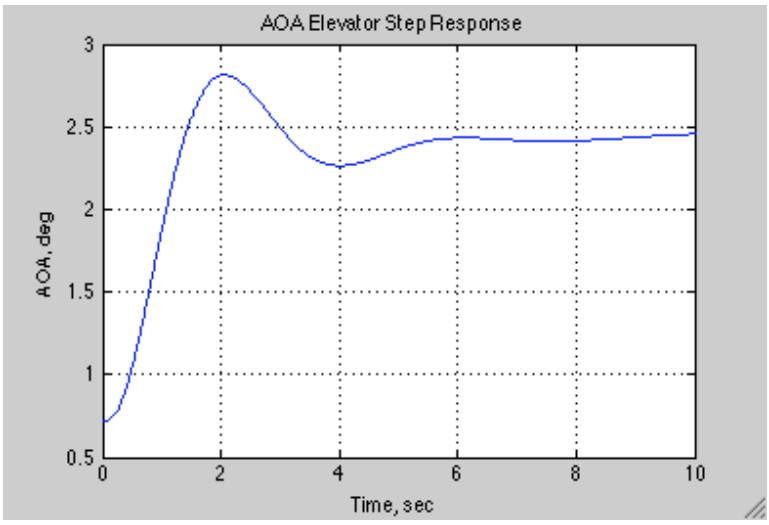

Figure, 4.1, Example Angle-of-Attack Step-H Response

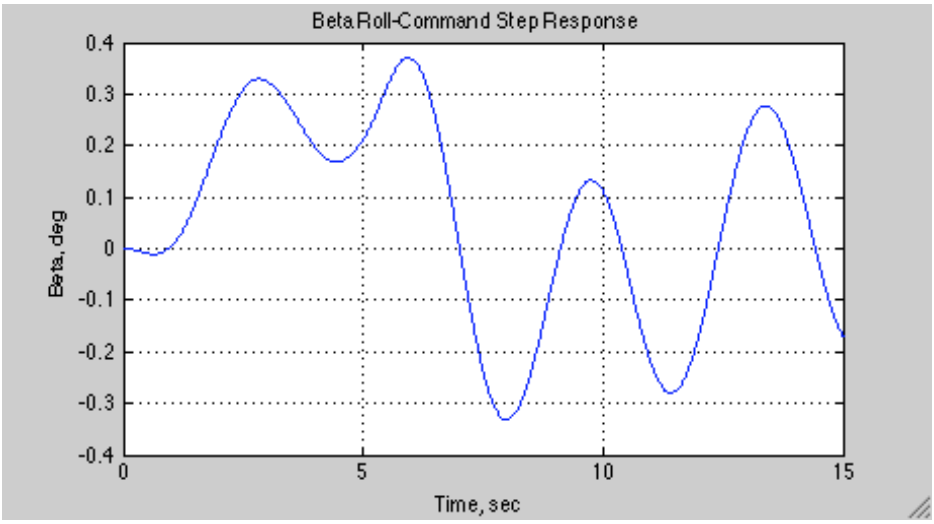

Figure, 4.2, Example Sideslip-Angle Roll-Doublet Response

The vehicle flight-path angle is defined as follows:

$$\gamma = \sin^{-1}\left(\frac{\dot{h}}{V_{\infty i}}\right) \tag{4.2}$$

Here, $\dot{h}$ is the inertial rate of climb and $V_{\infty i}$ is the vehicle's inertial velocity, or the velocity of the vehicle with respect to the Earth as given in Eqns. (3.1). The *i* subscript is added here to remind the reader that this quantity is not the velocity of the vehicle with respect to the atmosphere if winds are present.

The sensed angular rates are given as follow:

$$P_{cg}(t) = P(t) + \sum_{i=4}^{5} \nu'_{T_i}(x_{cg})\dot{\eta}_i(t)$$
$$Q_{cg}(t) = Q(t) + \sum_{i=1}^{3} \nu'_{Z_i}(x_{cg})\dot{\eta}_i(t) \tag{4.3}$$
$$R_{cg}(t) = P(t) + \sum_{i=4}^{5} \nu'_{Y_i}(x_{cg})\dot{\eta}_i(t)$$

where the terms $\nu'_{\bullet}(x_{cg})$ are angular displacements in the appropriate vibration mode shapes, evaluated at the c.g location.* The first, or $\nu'_{T_i}(x_{cg})$, is the torsional deformation of the fuselage taken about the vehicle *X* axis in the mode shape of the *i*'th anti-symmetric vibration mode. Likewise, $\nu'_{Z_i}(x_{cg})$ is the bending deformation of the fuselage taken about the vehicle *Y* axis, or the slope of the *Z*-displacements, in the mode shape of the *i*'th symmetric vibration mode. Finally, $\nu'_{Y_i}(x_{cg})$ is the bending deformation of the fuselage taken about the vehicle *Z* axis, or the slope of the *Y*-displacements, in the mode shape of the *i*'th anti-symmetric vibration mode. The terms $\dot{\eta}_i(t)$ are the modal velocities, or the rate of change of the generalized coordinate associated with the *i*'th (symmetric or anti-symmetric) vibration mode.

Two examples of angular-rate responses obtained from The Simulation are shown in Figs. 4.3 and 4.4. The same initial trim flight condition and the same two inputs considered previously are used, a negative-one-degree step commanded symmetric-horizontal-tail deflection and a one-degree doublet commanded blended roll command. The first figure shows the pitch-rate response, measured at the c.g., while the second shows the roll-rate response, also measured at the c.g.

* It is important to note that with elastic deformations, the c.g. is no longer fixed to a material point on the vehicle. So when we say, "measured at the c.g.," we mean measured at the c.g. location of the undeformed vehicle.

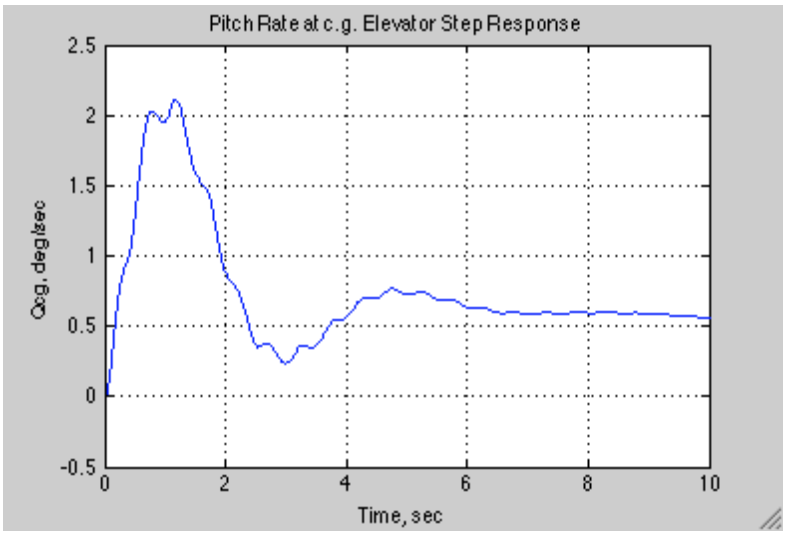

Figure 4.3, Pitch-Rate (at c.g.) Step-H Response

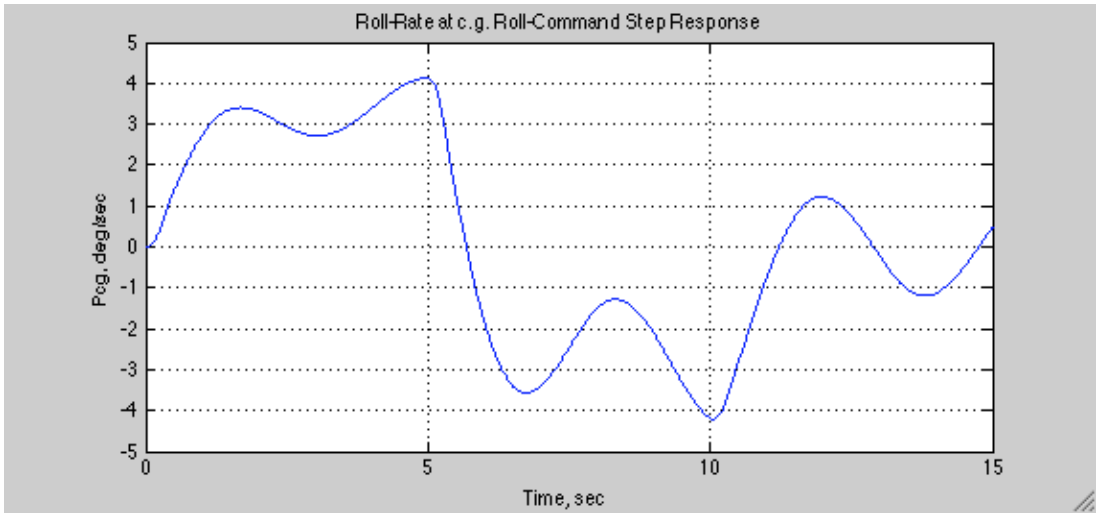

Figure 4.4, Roll-Rate (at c.g.) Doublet-Roll-Command Response

The sensed accelerations at the c.g. are given as

$$n_{Y\,cg}(t) = n_{Y\,cg\,RB}(t) + \sum_{i=4}^{5} v_{Y_i}(x_{cg})\ddot{\eta}_i(t)$$
$$n_{Z\,cg}(t) = n_{Z\,cg\,RB}(t) + \sum_{i=1}^{3} v_{Z_i}(x_{cg})\ddot{\eta}_i(t) \qquad (4.4)$$

where the terms $v_{\bullet_i}(x_{cg})$ are the Y or Z displacements in the i'th anti-symmetric or symmetric vibration mode shape, respectively, measured at the c.g. These sensed accelerations are also

functions of the Y and Z accelerations of the c.g. associated with the rigid-body degrees of freedom. These two accelerations are given as

$$\begin{aligned} n_{Y\,cg\,RB}(t) &= \dot{V} + RU - PW - g\cos\theta\sin\phi \\ n_{Z\,cg\,RB}(t) &= \dot{W} + PV - QU - g\left(\cos\theta\cos\phi - 1\right) \end{aligned} \tag{4.5}$$

In the second of these expressions, the negative 1 in the last parentheses indicates that the vertical acceleration is being measure from a 1-g trim flight condition.

Two example acceleration responses obtained from The Simulation are shown in Figs. 4.5 and 4.6. The same initial trim flight condition and the same two inputs considered previously are used here, a negative-one-degree step commanded symmetric-horizontal-tail deflection and a one-degree doublet commanded blended roll command. The first figure shows the plunge-acceleration n_Z response, measured at the c.g., while the second shows the lateral-acceleration n_Y response, also measured at the c.g.

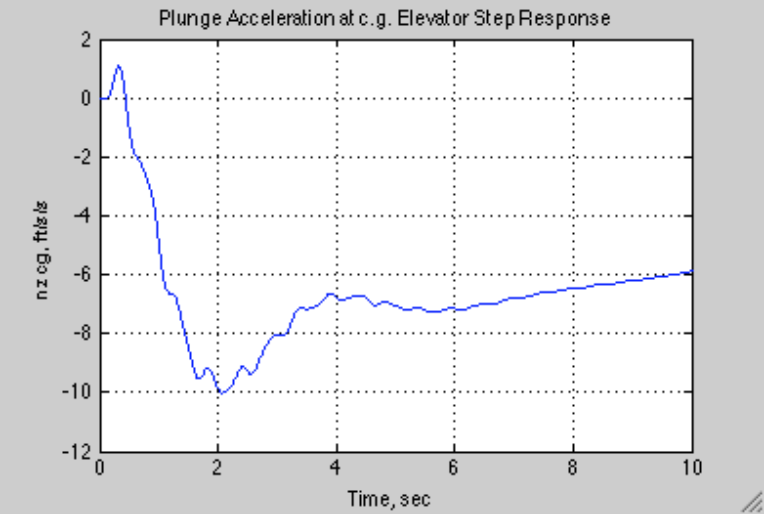

Figure 4.5, Plunge-Acceleration (at c.g.) Step-H Response

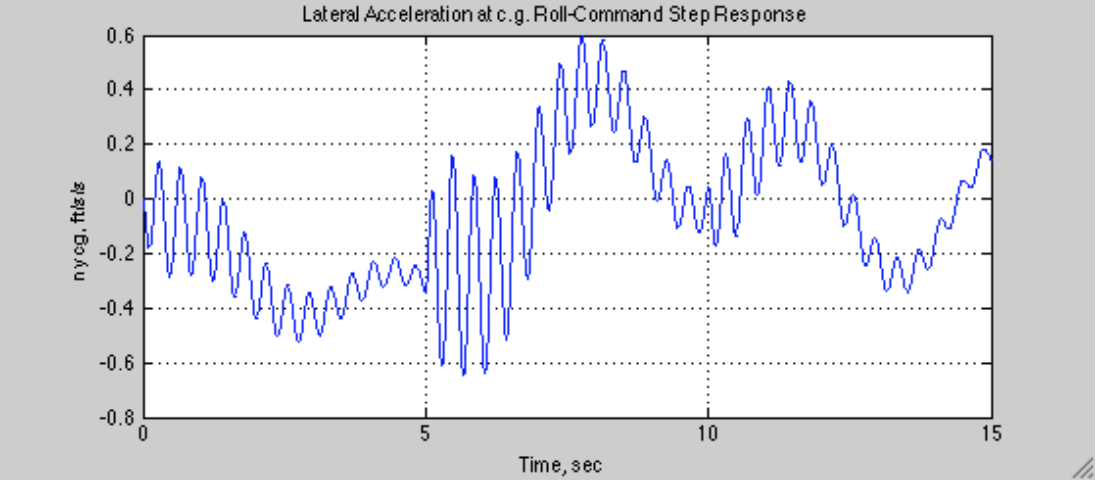

Figure 4.6, Lateral-Acceleration (at c.g.) Roll-Doublet- Response

The sensed accelerations at the cockpit/control vanes are given as

$$n_{Y\,cp}(t) = n_{Y\,cg\,RB}(t) + l_X\left(\dot{R} + PQ\right) + \sum_{i=4}^{5} v_{Y_i}(x_{cv})\ddot{\eta}_i(t)$$
$$n_{Z\,cp}(t) = n_{Z\,cg\,RB}(t) - l_X\left(\dot{Q} - PR\right) + \sum_{i=1}^{3} v_{Z_i}(x_{cv})\ddot{\eta}_i(t) \qquad (4.6)$$

These accelerations are seen to depend on the "rigid-body" accelerations, given by Eqns. (4.5). In addition, they also contain contributions from the elastic degrees of freedom, similar to the summation terms in Eqns. (4.5). However, the summations in Eqns. (4.6) are functions of the *Y* and *Z* displacements in the respective mode shapes, measured at the location of the control vanes. (The vanes are actually a small distance in front of the cockpit, but for our purposes the vanes and cockpit are taken to be co-located.) Finally, the accelerations at the control vanes are seen to depend on l_X, which is the axial (*X*) distance between the vanes and the c.g. In this study, this distance is 69.7 ft.

Two example acceleration responses obtained from The Simulation are shown in Figs. 4.7 and 4.8. The same initial trim flight condition and the same two inputs considered previously are used here, a negative-one-degree commanded symmetric-horizontal-tail deflection and a one-degree doublet commanded blended roll command. The first figure shows the plunge-acceleration response, measured at the control vane/cockpit, while the second shows the lateral-acceleration response, also measured at the control vane/cockpit. Elastic response is evident.

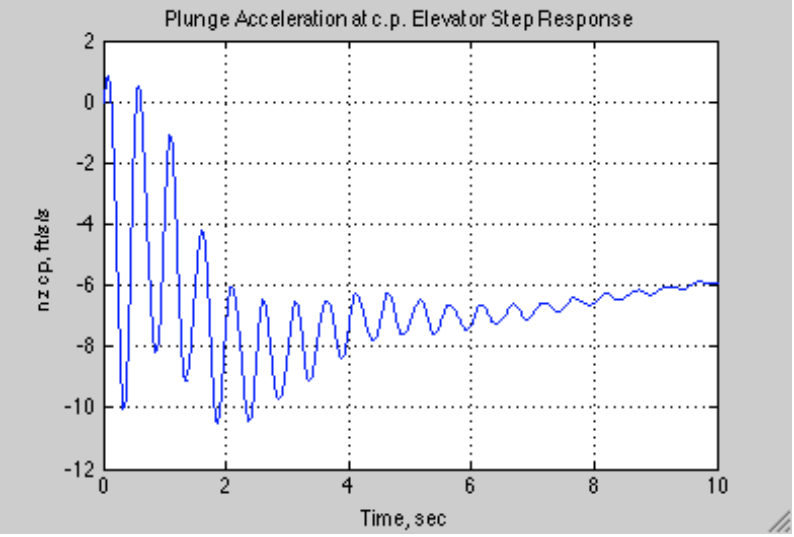

Figure 4.7, Plunge-Acceleration (at cp) Step-H Response

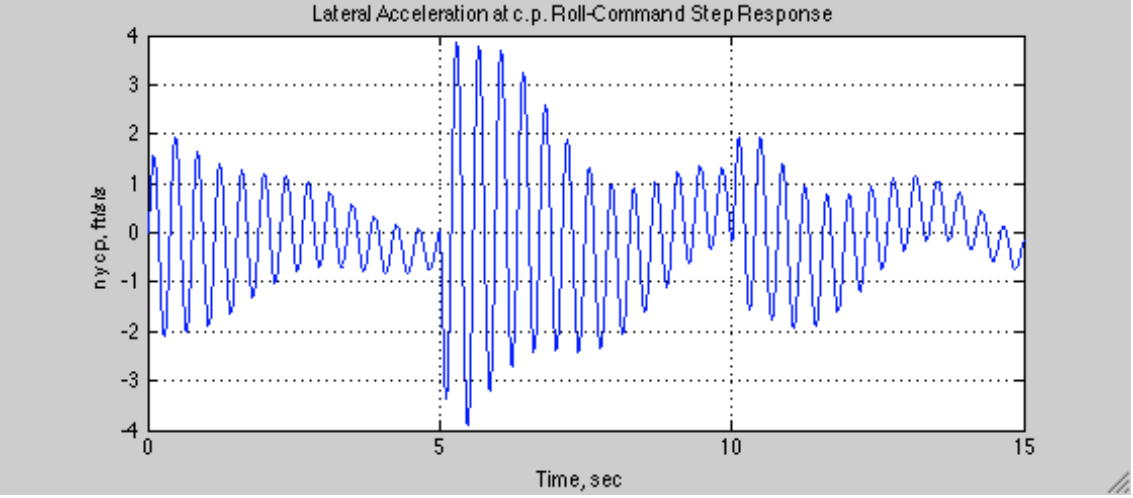

Figure 4.8, Lateral-Acceleration (at cp) Roll-Doublet Response

5. Engine, Actuators, and Limiters

Models for the engine and surface-actuator dynamics are included in The Simulation, and were obtained from [Waszak, Davidson, and Schmidt (1987)] and/or [Wykes, Byar, MacMiller, and Greek (1980)]. The Simulink model for the engine is shown in Fig. 5.1. The input to the engine is the power-lever angle PLA (e.g., from the cockpit). The model includes an engine rate limit, which limits the rate of change of engine thrust, maximum and minimum limits on the power-lever angle, and a database providing the achievable engine thrust as a function of PLA, altitude, and Mach number. The maximum and minimum PLA limits correspond to fight idle and maximum thrust without afterburner, respectively.

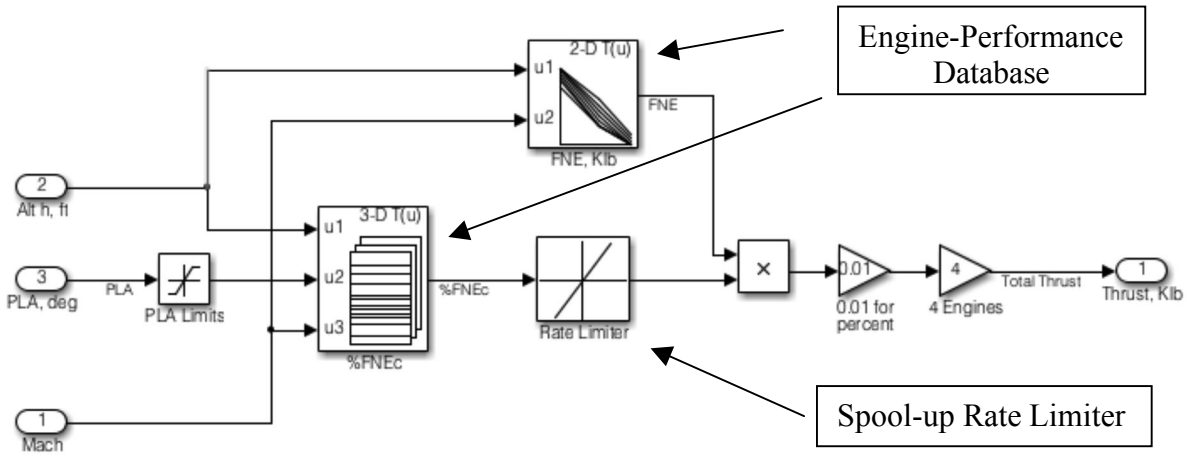

Figure 5.1, Simulation Diagram for Engine Dynamics and Achievable Thrust

Consistent with [Waszak, Davidson, and Schmidt (1987)] and/or [Wykes, Byar, MacMiller, and Greek (1980)], the models for the dynamic response of all surface actuators and control servos are first-order lags. The lag time constants and deflection limits for the various control surfaces and servos are listed in Table 5.1. Note that the control-vane deflection limit of ± 20 deg has an asterisk. This is due to the fact that the vane aerodynamic model includes a vane-stall limit of +15/-35 deg local angle of attack.

Table 5.1, Actuator and Servo Time Constants and Deflection Limits

Surface	**Time Constant**	**Deflection Limits**	**Surface**	**Time Constant**	**Deflection Limits**
Horizontal Tail, H	0.1 sec	10 -20 deg	Upper Rudder, RU	0.1 sec	± 10 deg
Horizontal Tail, DH	0.1 sec	Fcn. of H ± 20 max.	Lower Rudder, RL	0.05 sec	± 10 deg
Spoilers, sp	0.1 sec	0-45 deg	Control Vanes, cv	0.02 sec	± 20 deg*
H Servo	0.0175 sec	-	Sp Servo	0.05 sec	-
DH Servo	0.05 sec	-	RL Servo	0.0125 sec	-

6. Effects of Atmospheric Turbulence

The models for the effects of turbulence are taken from [Schmidt (2012)] and [Waszak, Davidson, and Schmidt (1987)]. The statistical model for the turbulence is the Dryden gust spectrum, generated by passing unit-intensity white noise through an appropriate filter. The transfer functions for the filters for the vertical and horizontal gust velocities, v_g and w_g , along with the values used for the parameters , are

$$G_{v_g}(s) \equiv \sigma_v \sqrt{\frac{L_v}{\pi U_0}} \frac{\left(1 + s\sqrt{3}L_v / U_0\right)}{\left(1 + sL_v / U_0\right)^2}$$
$$G_{w_g}(s) \equiv \sigma_w \sqrt{\frac{L_w}{\pi U_0}} \frac{\left(1 + s\sqrt{3}L_w / U_0\right)}{\left(1 + sL_w / U_0\right)^2} \tag{6.1}$$

where U_0 = reference velocity = 659 fps (default)

L_V = characteristic length = 1750 ft

$\sigma_.$ = rms gust intensities = 6 fps (default) ("moderate turbulence")

It is noted that these two transfer functions are the same if the same rms gust intensities and characteristic lengths are used. The Simulation user may desire to adjust three of the above parameters, the reference flight velocity U_0 and the rms gust intensities $\sigma_.$ For example, even though the user may be interested in simulating a flight condition with a trim flight velocity other than 659 fps, they may wish to hold U_0 at 659 fps to keep the gust spectrum constant, for run-to-run comparisons.

The unit-intensity white-noise excitation is generated in The Simulation by a Simulink block that generates band-limited white noise. The sample-time parameter set in this noise block is set to 0.005 sec, which should be appropriate, given the time constants of the subsystems in The Simulation. But smaller sample times may be used if desired, though the simulation executes more slowly. The white-noise sequences from the two noise blocks used depend on the random-number seed set in the blocks' parameters, and the two seeds should be two uncorrelated random numbers to assure that the white-noise sequences are uncorrelated. But by keeping the two seeds constant (not necessarily equal to each other) over various simulations, one is assured of using the same turbulence sequence, which allows more meaningful run-to-run comparisons.

The gust velocities v_g and w_g are assumed to be horizontal and vertical, respectively, with reference to Earth-fixed coordinates. But the vertical and lateral gusts in the vehicle-fixed coordinate frame V_g and W_g are needed. Using the Euler angles, these gusts in the vehicle-fixed frame are

$$\begin{aligned} V_g &= v_g \cos\phi + w_g \sin\phi \cos\theta \\ W_g &= -v_g \sin\phi + w_g \cos\phi \cos\theta \end{aligned} \tag{6.2}$$

Given these gust velocities V_g and W_g, the models for the effects of turbulence may now be developed. Recall that the vehicle's inertial velocity is $V_{\infty i}$, a function of *U, V,* and *W*. Now define the velocity of the vehicle with respect to the air mass through which it is traveling to be

$$\begin{aligned} \mathbf{V}_{\infty a} &= U_a \mathbf{i}_V + V_a \mathbf{j}_V + W_a \mathbf{k}_V \\ V_{\infty a} &= \sqrt{U_a^2 + V_a^2 + W_a^2} \end{aligned} \tag{6.3}$$

where

$$\begin{aligned} U_a &= U \\ V_a &= V + V_g \\ W_a &= W + W_g \end{aligned}$$

And the instantaneous angles of attack and sideslip, and their rates, are functions of the above components of velocity. That is,

$$\begin{aligned} \alpha &= \tan^{-1}\left(\frac{W_a}{U_a}\right) & \dot{\alpha} &= \frac{U_a \dot{W}_a - W_a \dot{U}_a}{U_a^2 + W_a^2} \\ \beta &= \sin^{-1}\left(\frac{V_a}{V_{\infty a}}\right) & \dot{\beta} &= \frac{V_{\infty a}\dot{V}_a - V_a \dot{V}_{\infty a}}{V_{\infty a}^2 \cos\beta} \\ & & \dot{V}_{\infty a} &= \left(U_a \dot{U}_a + V_a \dot{V}_a + W_a \dot{W}_a\right) / V_{\infty a} \end{aligned} \tag{6.4}$$

And of course, the aerodynamic forces and moments given in Eqns. (3.3 and 3.5) are functions of these quantities.

Shown in Figs. 6.1 and 6.2 are two example turbulence responses, lateral and vertical accelerations measured at the cockpit with the vehicle excited only by turbulence. There are no external control commands, and the SAS's and SMCS's are all inactive. As before, the initial trim flight condition is Mach = 0.6, h = 5000 ft., and moderate turbulence with rms gust

velocities of 6 fps are used. The participation of the first (symmetric) and fifth (anti-symmetric) aeroelastic modes are evident in these responses. (Note the differences between the vertical scales of the plots.)

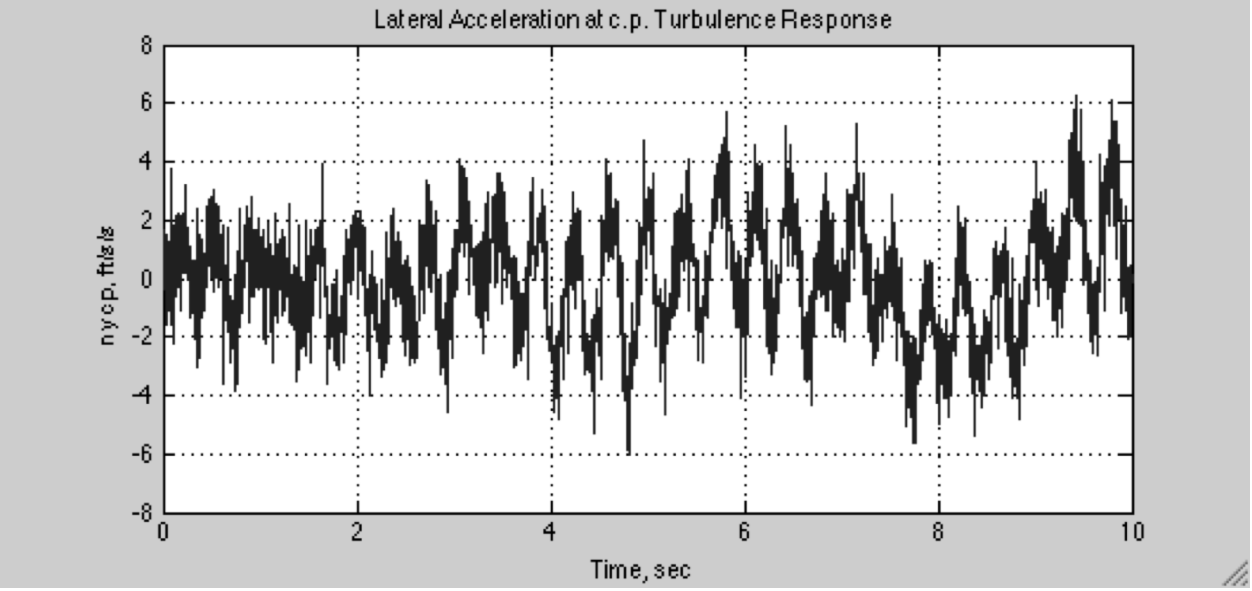

Figure 6.1, Lateral Cockpit-Acceleration Turbulence Response

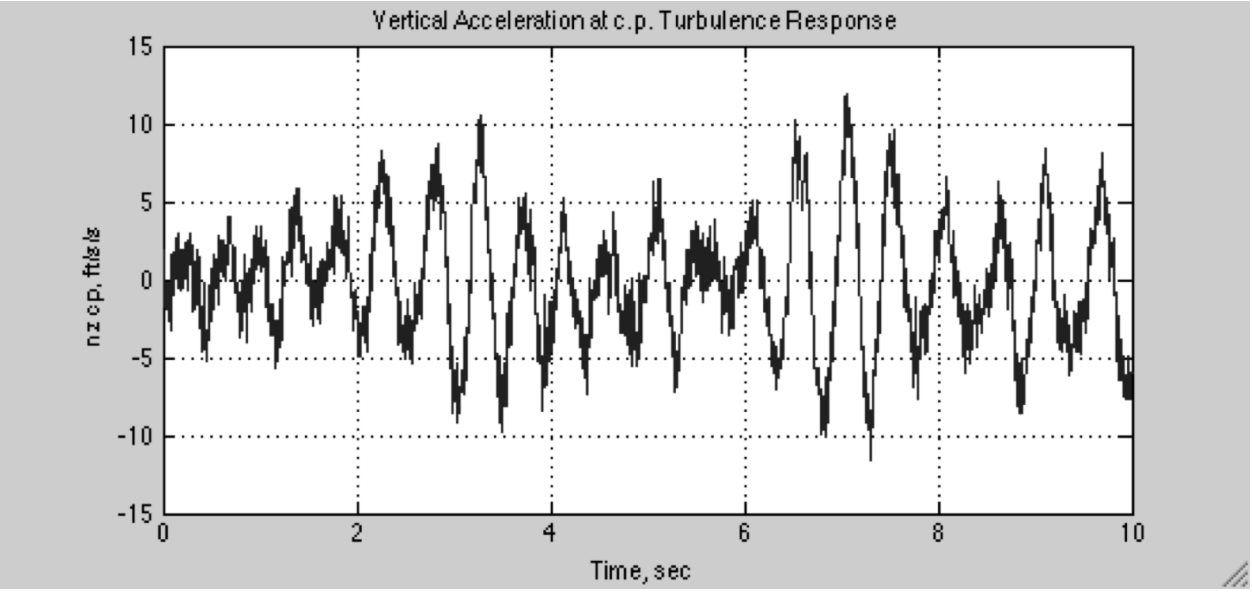

Figure 6., Vertical Cockpit-Acceleration Turbulence Response

7. Stability Augmentation Systems

The Simulation includes three stability augmentation systems, a pitch SAS, a roll SAS, and a yaw SAS. All three of these systems are based on those on the B-1, as documented in [Waszak, Davidson, and Schmidt (1987)] and [Wykes, Byar, MacMiller, and Greek (1980)]. The roll and yaw SAS's were essentially unchanged from those given in these references, but the pitch SAS was modified. In addition, the portions of the three B-1 SAS's related specifically to manual control, such as non-linear stick gearing, are not included or have been simplified in the SAS's in The Simulation.

The pitch SAS on the B-1 incorporated both acceleration and pitch-rate feedback to primarily adjust the short-period frequency and damping. But during our analysis of the pitch SAS and the vertical SMCS, it was decided to only use a pitch damper and to slightly adjust the pitch-rate feedback gain. These adjustments allowed for increased performance to be obtained from the SMCS (discussed in Section 8). The Simulink diagram for the pitch SAS, as modified, is shown in Fig. 7.1. The SAS feeds back pitch rate, measured at the c.g., to the horizontal-tail actuator, and includes the adjusted pitch-rate feedback gain, scheduled with altitude, plus a manual switch. This switch allows the user to activate or deactivate the SAS.

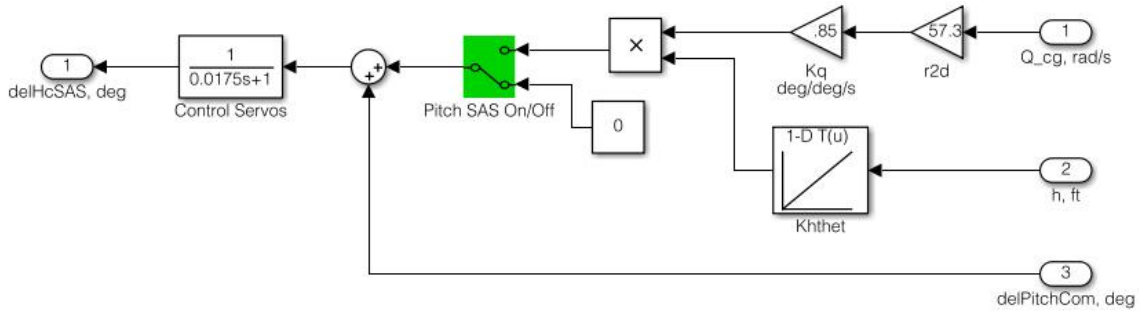

Figure 7.1, Simulation Diagram of the Pitch SAS

Examples of vehicle pitch-rate step responses are shown in Figs. 7.2 and 7.3. Shown are the responses to a negative one-degree commanded horizontal-tail deflection, with and without the pitch SAS active. The initial, trim flight condition is at Mach = 0.6, h = 5000 ft. Figure 7.2 shows the responses of the rigid-body pitch rate, which cannot be sensed directly, while Fig. 7.3

shows the responses of the pitch rate measured at the c.g. Increased short-period damping is evident with the SAS active.

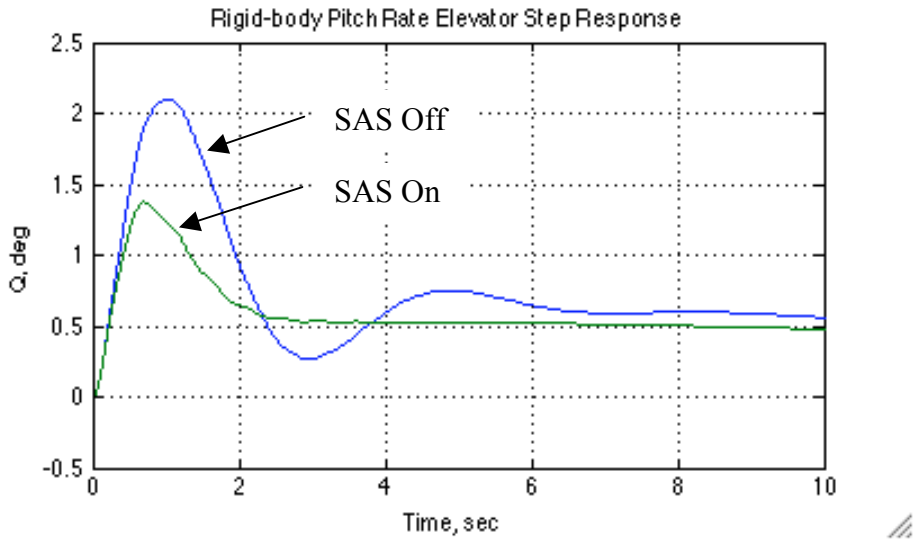

Figure 7.2, Rigid-Body Pitch-Rate Step Responses, With and Without Pitch SAS

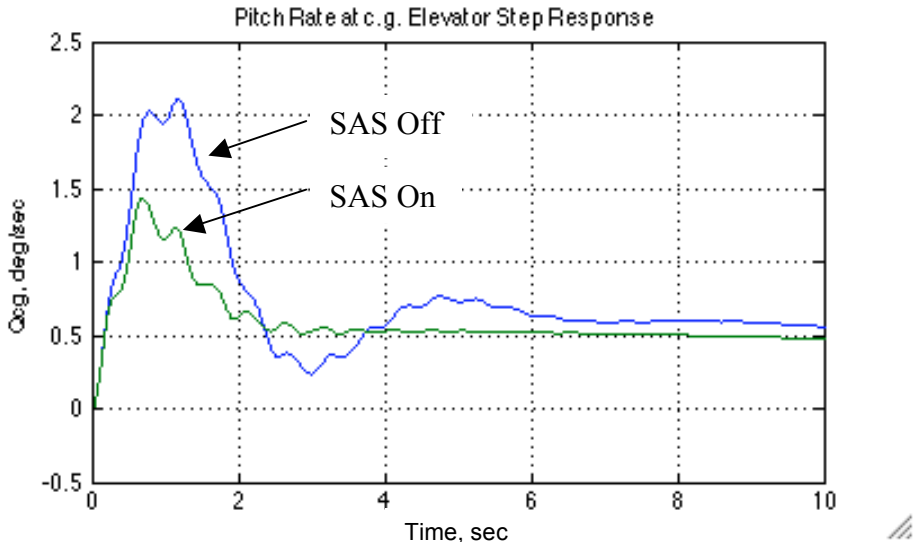

Figure 7.3, Pitch-Rate (at c.g.) Step Responses, With and Without Pitch SAS

The Simulink diagrams for the roll and yaw SAS's are shown in Fig. 7.4. The roll SAS is a constant-gain roll damper, feeding back roll rate measured at the c.g. to commanded differential horizontal-tail deflections. A manual switch is included to allow the user to activate

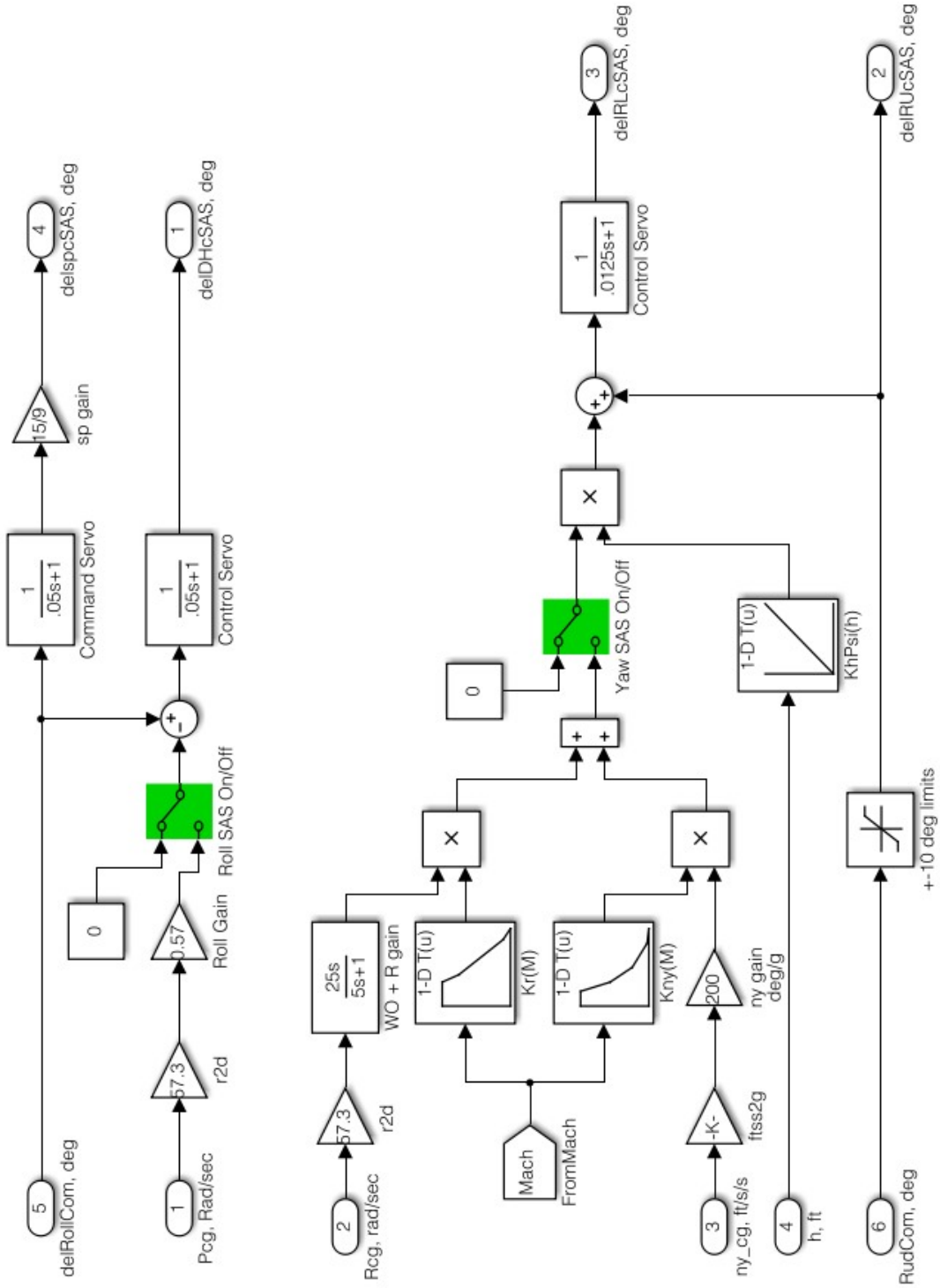

Figure 7.4, Simulations Diagram for the Roll and Yaw SAS

and deactivate the SAS. A roll command is the second input to the roll SAS, and generates parallel commands to the differential-tail and spoiler actuators. This input would have originally resulted from pilot lateral stick deflection.

The yaw SAS is a gain-scheduled yaw damper, feeding back washed-out yaw rate and lateral acceleration, both measured at the c.g., to command lower-rudder deflections. Both yaw-rate and lateral-acceleration gains are scheduled on Mach number and altitude. A manual switch is included to allow the user to activate and deactivate the SAS. The SAS also acts on a rudder-command input (originally originating from cockpit pedal deflections), generating parallel commands to the upper- and lower-rudder actuators.

It has been noted that the portions of the roll and yaw SAS's dealing specifically pilot control-inputs have been simplified. For example, shown in Fig. 7.5 is the block diagram of the B-1 roll SAS taken from [Waszak, Davidson, and Schmidt (1987)]. The blocks that were eliminated or modified in The Simulation are noted.

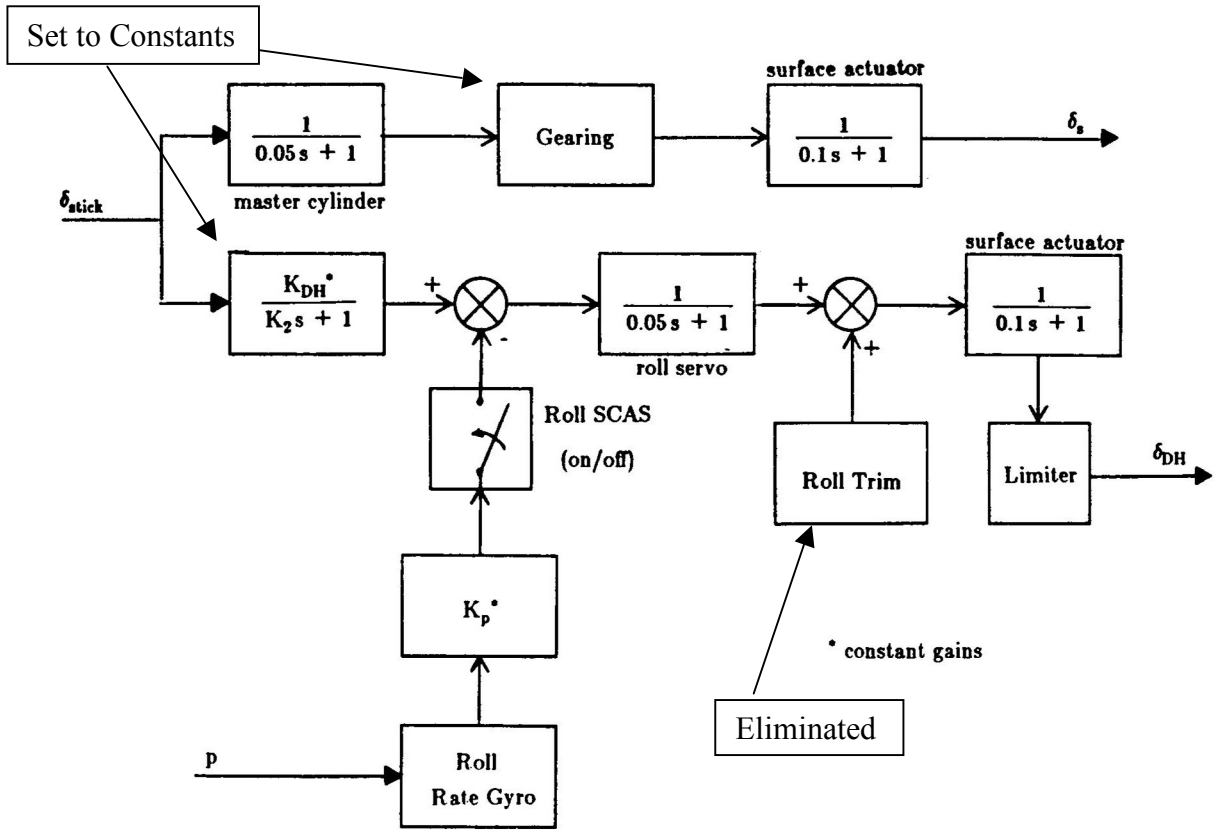

Figure 7.5, Block Diagram of B-1 Roll SAS, From [Waszak, Davidson, and Schmidt (1987)].

Two examples of the vehicle's roll-rate responses to the roll-command one-degree doublet into the roll SAS are shown in Fig. 7.6. The doublet consists of an initial one-degree command, followed by a two-degree reversal at five seconds, followed by a return to neutral at 10 seconds. The trim flight condition is again Mach = 0.6, h = 5000 ft. The responses shown are the roll rate, measured at the c.g., with and without the roll and yaw SAS's active. Clearly, these SAS's are effective at increasing Dutch-roll damping.

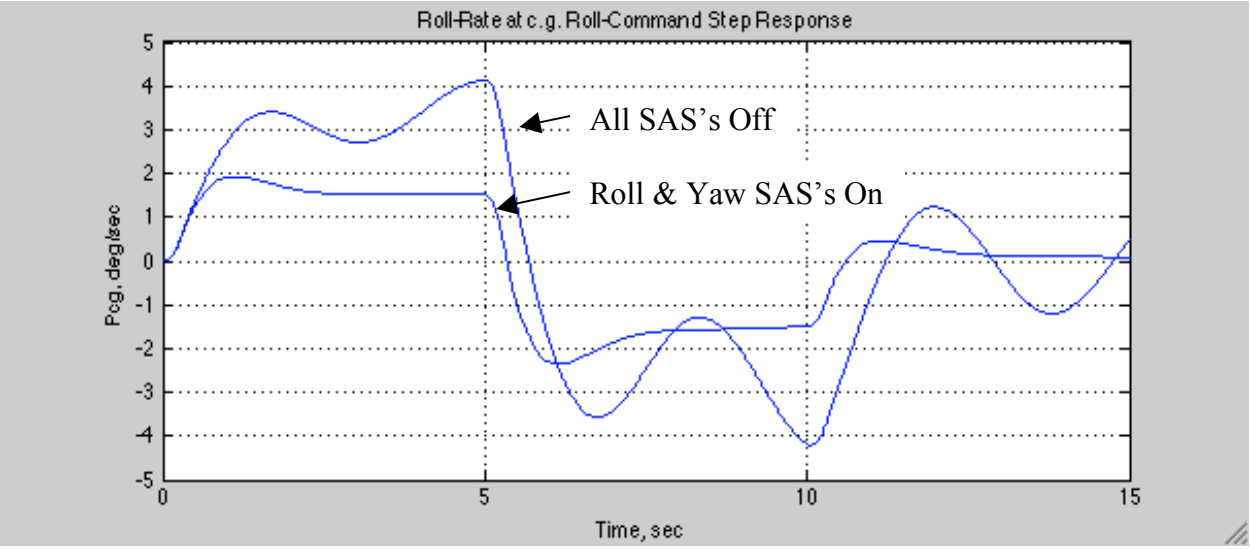

Figure 7.6, Roll Rate (at c.g.) Responses to Roll-Command Doublet, With and Without SAS's

8. Structural Mode Control Systems

The Simulation includes two active structural-mode control systems, one each to attenuate vertical and lateral cockpit accelerations. Such systems were employed on the B-1, rather than stiffening the structure, to save weight and to improve pilot ride quality. Both of the SMCS's included in The Simulation are based on those on the B-1, as documented in [Wykes, Borland, Klepl, and MacMiller (1977)] and [Wykes, Byar, MacMiller, and Greek (1980)]. The lateral SMCS is essentially unchanged from that given in the references, with only a slight gain adjustment. The vertical SMCS architecture remains as given in the references, but the compensation as well as the gains were modified.

The two SMCS's on the B-1 were developed using the concept known as identically located accelerometer and force (ILAF) put forth by Wykes. See [Wykes, Borland, Klepl, and MacMiller, (1977)]. Wykes showed that if the local velocity measured at the point of application of a force on a vibrating structure was fed back to the force effector, the damping of all the vibration modes would be increased. This concept became known later in the spacecraft community as the concept of co-located actuators and sensors.

It is important to also note a key design requirement for the B-1's SMCS's, that they not significantly affect the handling qualities of the vehicle (i.e., the performance of the SAS"s.). This requirement was carried over in the SMCS's developed in The Simulation. The B-1 SMCS's were also designed to only operate for a short time, and the pilot could both adjust the loop gain in each axis, as well as entirely disengage the SMCS's. Shown in Fig. 8.1 are three purely rigid-body pitch-rate step responses to a negative-one-degree commanded horizontal tail deflection, obtained from The Simulation. (Recall that this response cannot be directly measured, but of course is available from simulation.) The two responses with the pitch SAS active, with and without the vertical SMCS active, are almost identical, demonstrating that this SMCS in The Simulation has little effect on this important vehicle response, as desired.

The Simulink diagrams for the lateral and vertical SMCS's in The Simulation are shown in Fig. 8.2. The lateral SMCS feeds back blended accelerometer measurements, and generates commands for anti-symmetric deflections of the forward control vanes. The two accelerations feed back are the lateral acceleration at the cockpit (or control vane) and at the c.g. The output of

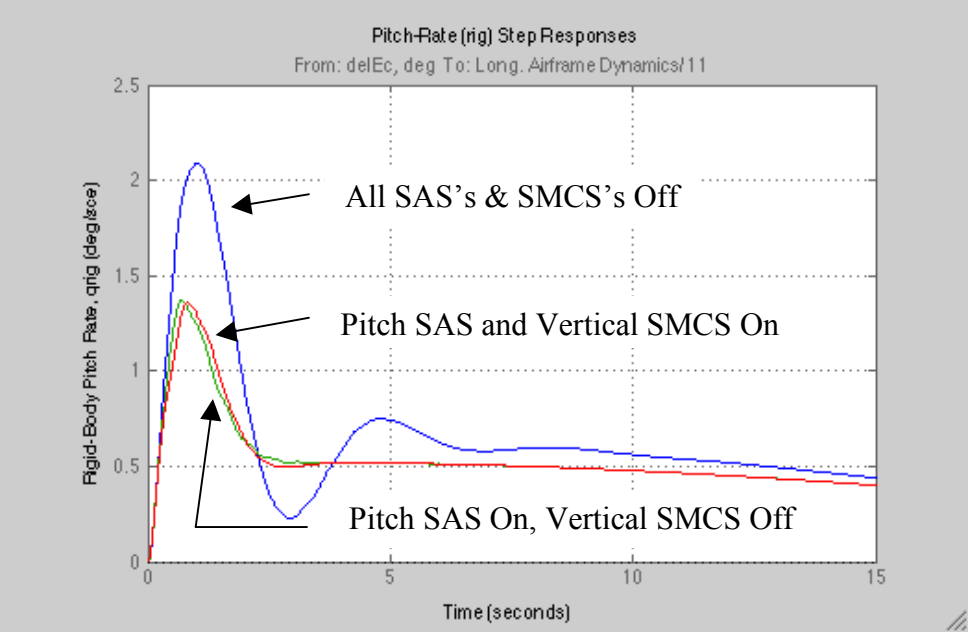

Figure, 8.1, Rigid-Body Pitch-Rate Step Responses, w/wo SAS, w/wo SMCS

the accelerometer at the c.g. is passed through a low-pass filter to attenuate high-frequency components, and thus attempt to filter out the contributions from the structural modes. So the blended signal tends to be rich in the elastic responses, rather than in the low-frequency rigid-body responses. These blended accelerations are then passed through a second low-pass filter, to generate a signal that approximates a sensed velocity. The filtered signal is then passed through a washout filter with a corner frequency below that of the lowest elastic mode, to achieve some decoupling between the actions of the SMCS and the roll and yaw SAS's. The feedback gain is scheduled on dynamic pressure.

Examples of cockpit-acceleration responses are shown in Figs. 8.3 and 8.4. The first shows the lateral cockpit accelerations in response to the one-degree, five-second roll-command doublet. Two responses are shown, one with no SAS's or SMCS's active, and one with only the lateral SMCS activated. Clearly the lateral SMCS attenuates this response. Shown in Fig. 8.4 are vertical accelerations in response to a commanded negative-one-degree-step horizontal-tail deflection. Again, two responses are shown, one with no SAS's or SMCS's active, and one with only the vertical SMCS activated. The effect of the SMCS on attenuating the acceleration is clearly evident.

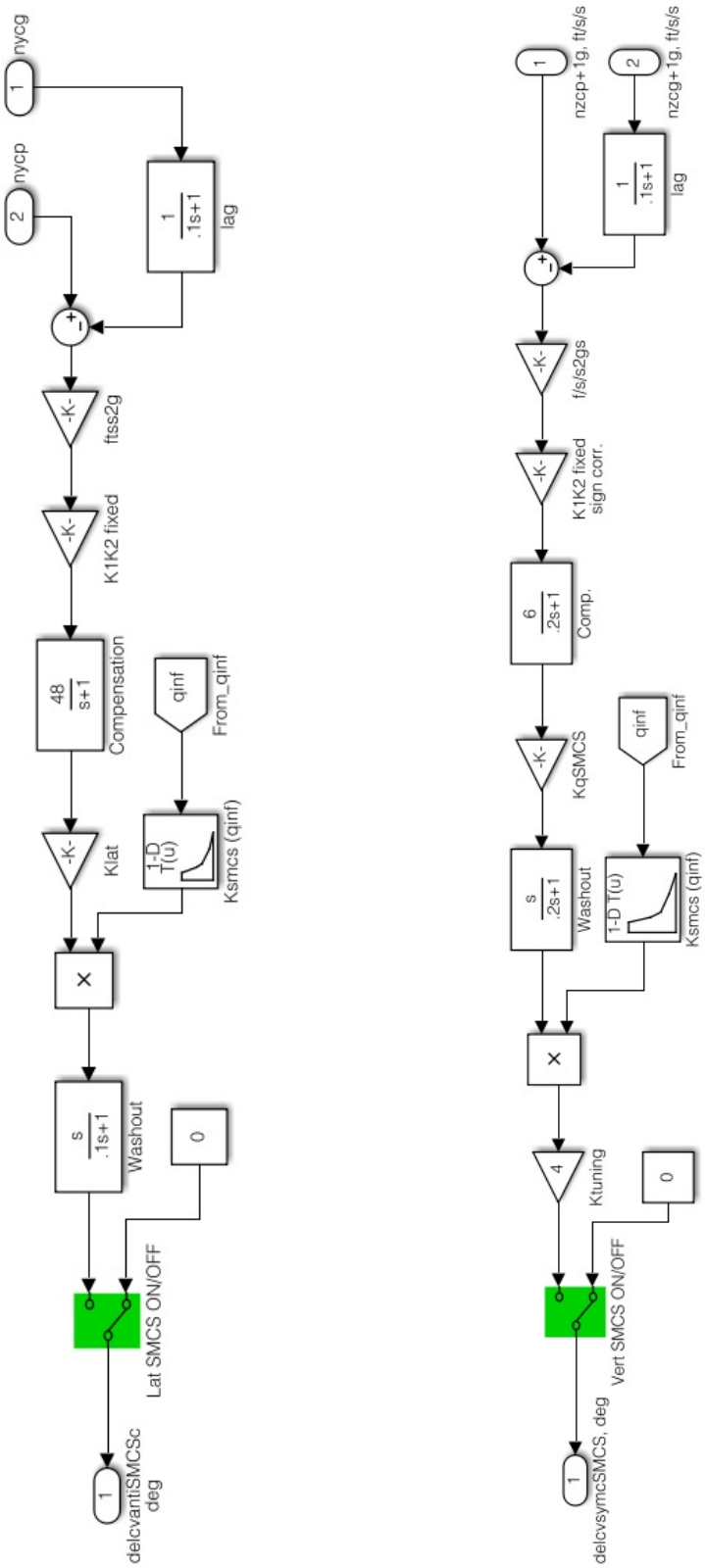

Figures 8.2, Simulation Diagrams for the Lateral and Vertical SMCS's

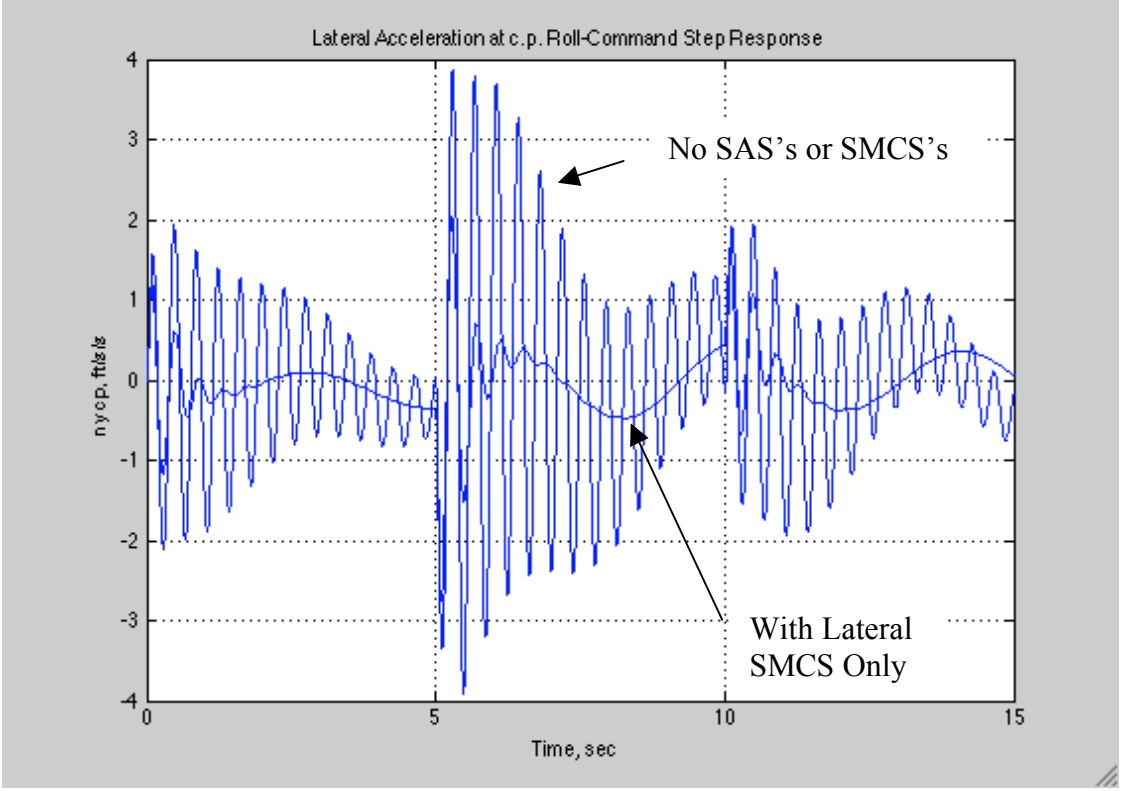

Figure 8.3, Lateral-Cockpit-Acceleration Response to Roll Doublet, With and Without SMCS

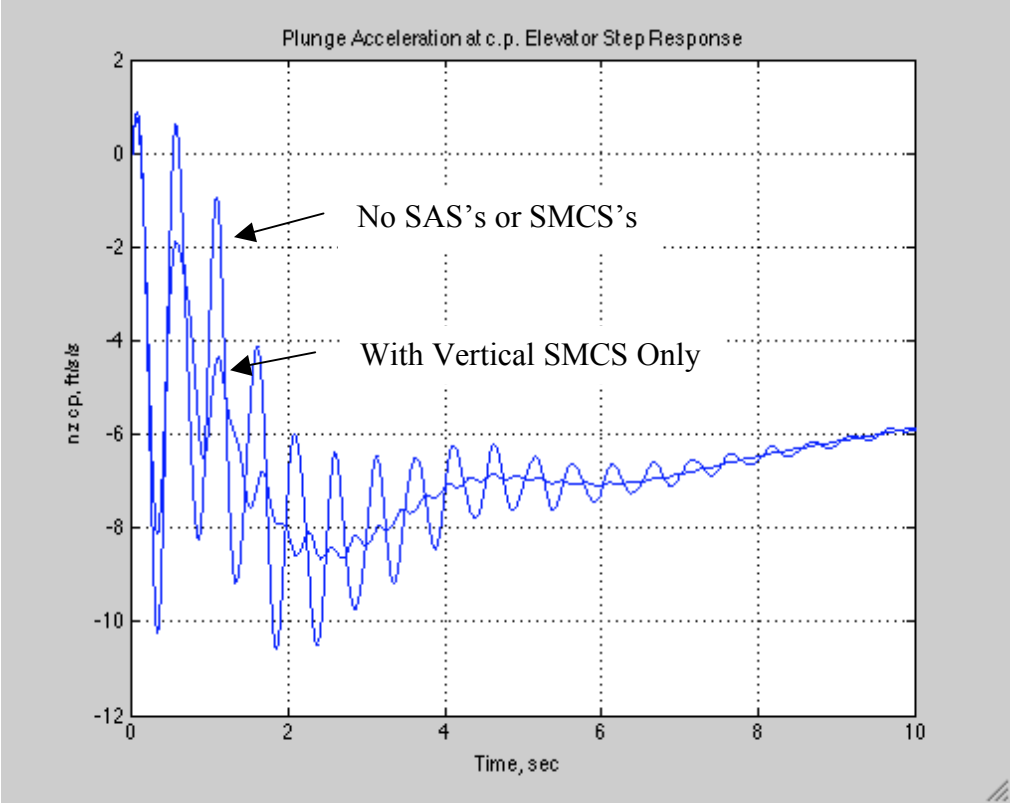

Figure 8.4, Vertical-Cockpit-Acceleration Step Responses, With and Without SMCS

9. Flight Envelope of Validity – Trim Analysis

The database in the engine model only extends to a Mach number of 0.8. Plus, the aerodynamic data does not extend much above this Mach number as well. These facts limit the maximum Mach number of validity to approximately 0.8. Additionally, the vehicle's static stability, as modeled, significantly degrades at angles of attack approaching stall, or at approximately 10 degrees. Finally, there are limits on maximum achievable engine thrust. These latter two factors limit the minimum flight velocities. Such considerations are the primary factors defining The Simulation's flight envelope. This flight envelope might be depicted as shown in Fig. 9.1. The approximate boundaries of the envelope are indicated by the black dashed lines, with a minimum altitude of 5000 ft.

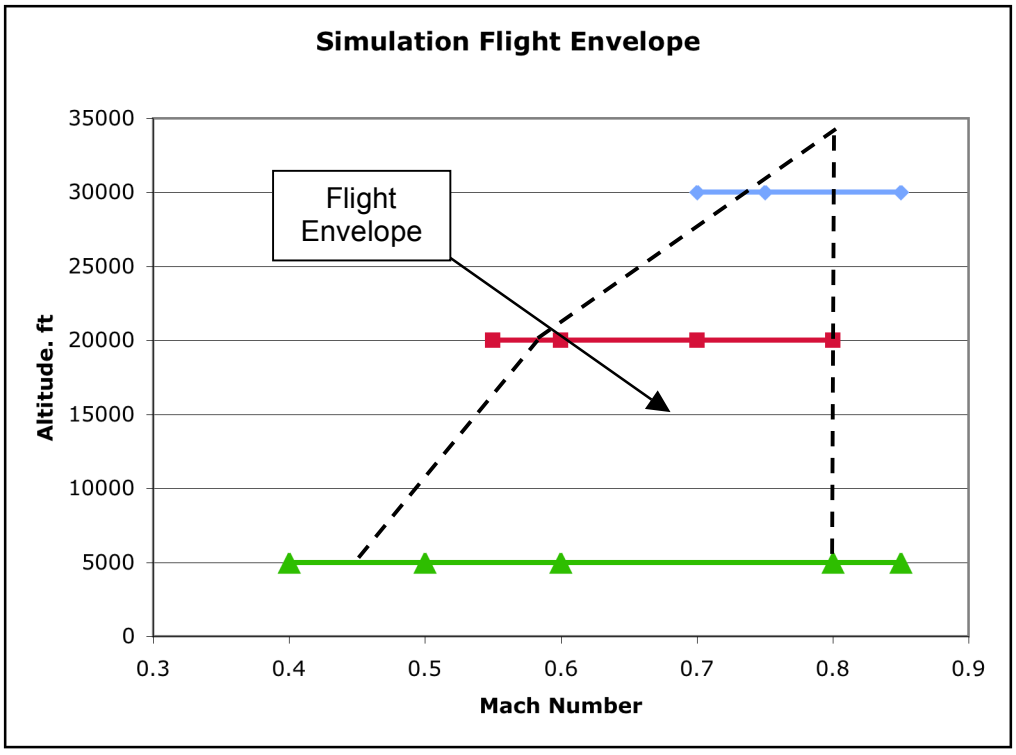

Figure 9.1, The Simulation Flight Envelope of Validity.

The data points appearing in Fig. 9.1 identify flight conditions (Mach and altitude) at which The Simulation has been trimmed in level flight. (But as noted, some of these flight

conditions lie outside the flight envelope, either due to stability limitations or to simulation-fidelity considerations.) We will now consider these trimmed conditions further.

The trim angle of attack at each flight condition is shown in Fig. 9.2, plotted as a function of trim Mach number. The data is plotted with Mach number decreasing because as Mach decreases, the required trim lift coefficient increases. Thus, this is also a plot of trim angle of attack vs. require trim lift coefficient. Note that to maintain static stability the maximum trim angle of attack must be less than 10 degrees, and the minimum trim flight Mach number at each altitude is indicated.

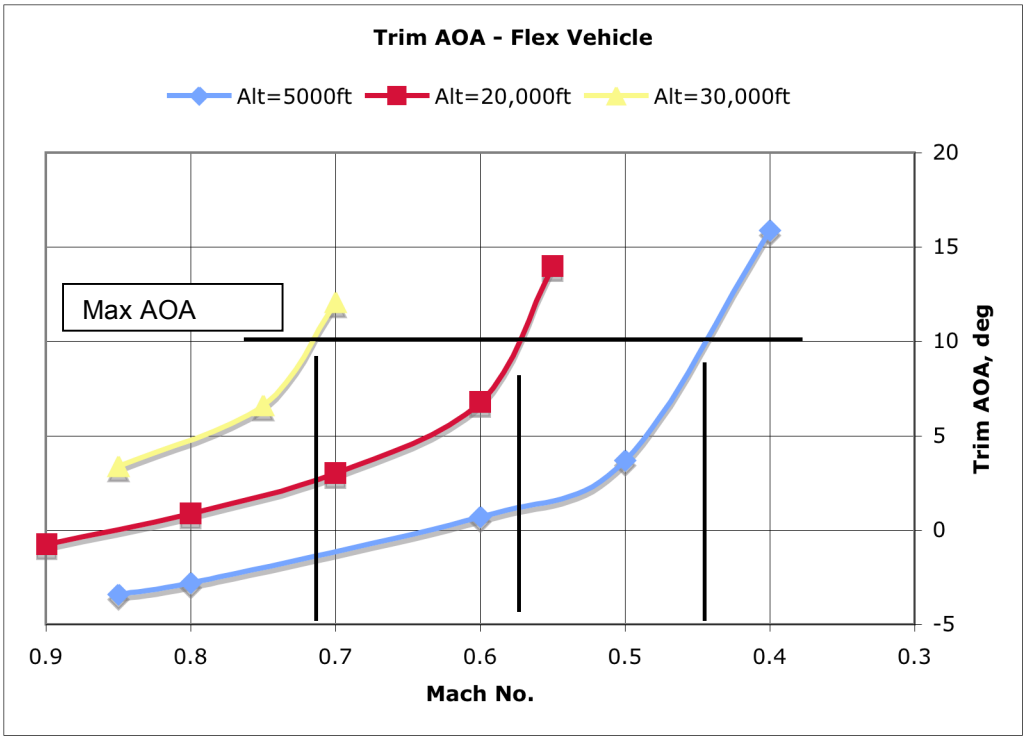

Figure, 9.2, Trim Angle of Attack

In addition, consider Fig. 9.3, which shows the require engine PLA setting as a function of trim Mach number. The maximum PLA setting for the engines is also indicated. This power maximum available also limits the minimum trim flight Mach number at each altitude, as indicated.

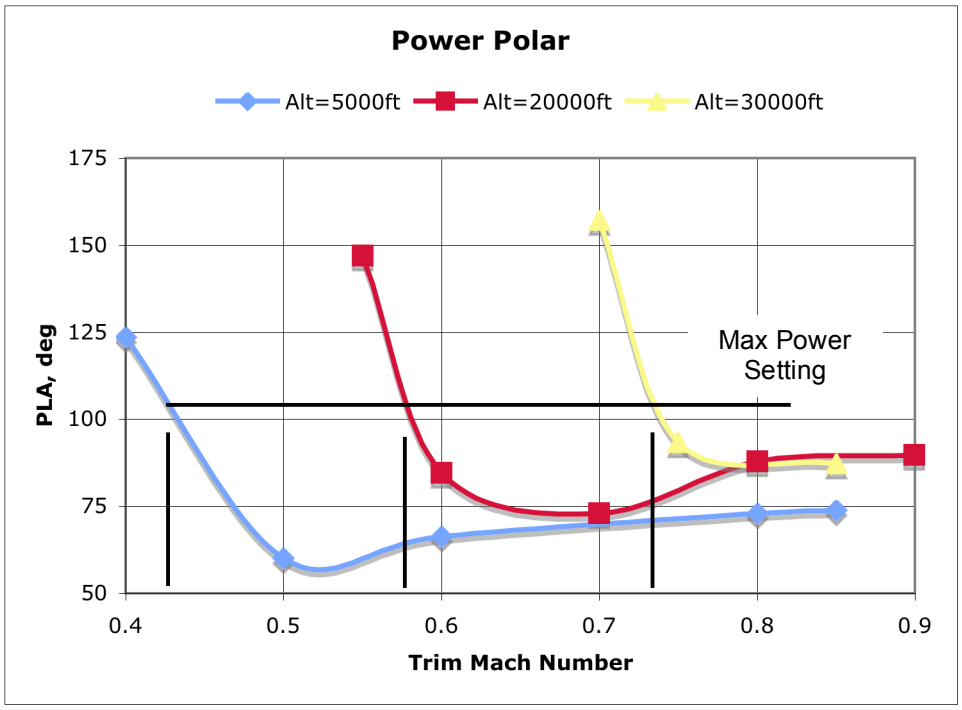

Figure 9.3, Require Power Lever Angle (Thrust) for Trim

Finally, the required trim-elevator (or horizontal tail) deflection is shown in Fig. 9.4, plotted as a function trim Mach number. Given that the maximum negative deflection of the horizontal tail is -20 degrees, these trim flight conditions do not violate this constraint.

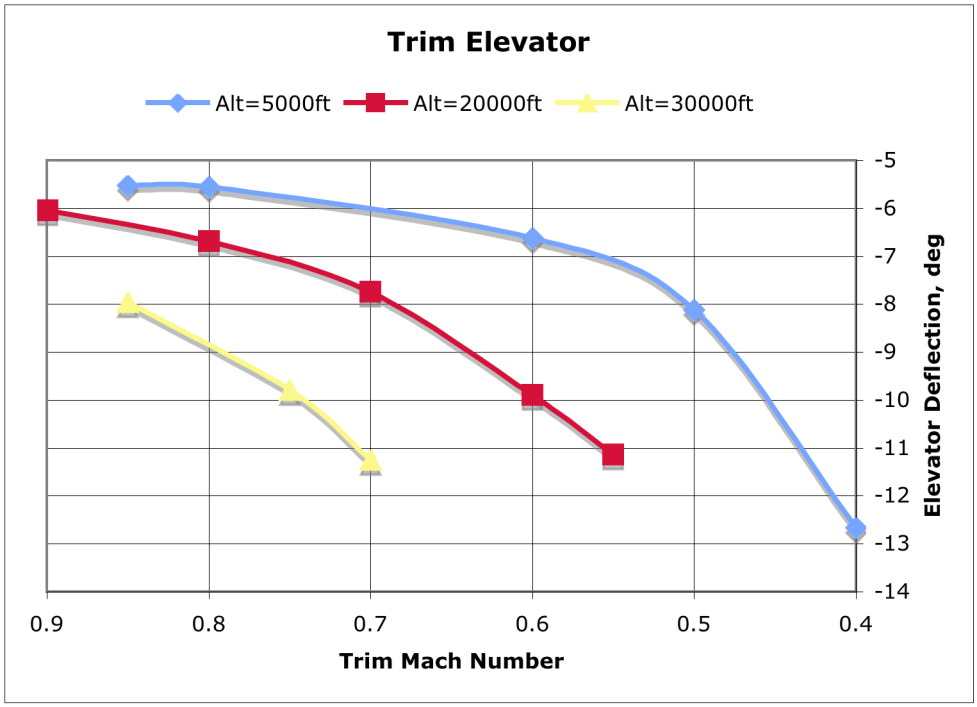

Figure 9. 4, Required Horizontal-Tail Deflection for Trim

10. References

1. Freeman and Rozsa, "Basic Modal Data Package for -55B Mid-Penetration Weight 65 Degree Wing Sweep," North American Aviation Memorandum VDD-71-4, Nov. 1971.
2. Schmidt, D. K. and Raney, D. L., "Modeling and Simulation of Flexible Flight Vehicles," *Journal of Guidance, Control, and Dynamics*, Vol. 24, No. 3, 1998, pp. 539–546.
3. Waszak, M. R. and Schmidt, D. K., "Analysis of Flexible Aircraft Longitudinal Dynamics and Handling Qualities," NASA Contractor Report CR-177943, 1985.
4. Waszak, M. R., Davidson, J. B., and Schmidt, D. K., "A Simulation Study of the Flight Dynamics of Elastic Aircraft, Results and Analysis," Vols. 1 and 2, NASA Contractor Report 4102, 1987.
5. Waszak, M. R. and Schmidt, D. K., "Flight Dynamics of Aeroelastic Vehicles*," Journal of Aircraft*, Vol. 25, No. 6, June 1988, pp. 563–571.
6. Waszak, M. R., Buttrill, C. S., and Schmidt, D. K., "Modeling and Model Simplification of Aeroelastic Vehicles: An Overview," NASA Technical Memorandum TM-107691, 1992.
7. Wykes, Borland, Klepl, and MacMiller, "Design and Development of a Structural Mode Control System," NASA Contractor Report CR-143846, Prepared by Rockwell International, Inc. October, 1977.
8. Wykes, Byar, MacMiller, and Greek, "Analyses and Test of the B-1 Aircraft Structural Mode Control System," NASA Contractor Report CR-144887, January, 1980.

Appendix – Users Manual

A conceptual block diagram of The Simulation is shown in Fig. A.1, and the boxes correspond to Simulink subsystems at the root level. The models contained in these subsystems have been described in the body of this report. In this Appendix, the necessary steps to set up and execute The Simulation will be described, and some sample results presented. The Simulation was developed in MATLAB 8.0, R2012b, and has not been tested on other versions as of yet. So this Users Manual is written assuming this version of MATLAB/Simulink is being used. If this is not the case, some modifications to the instructions may be required.

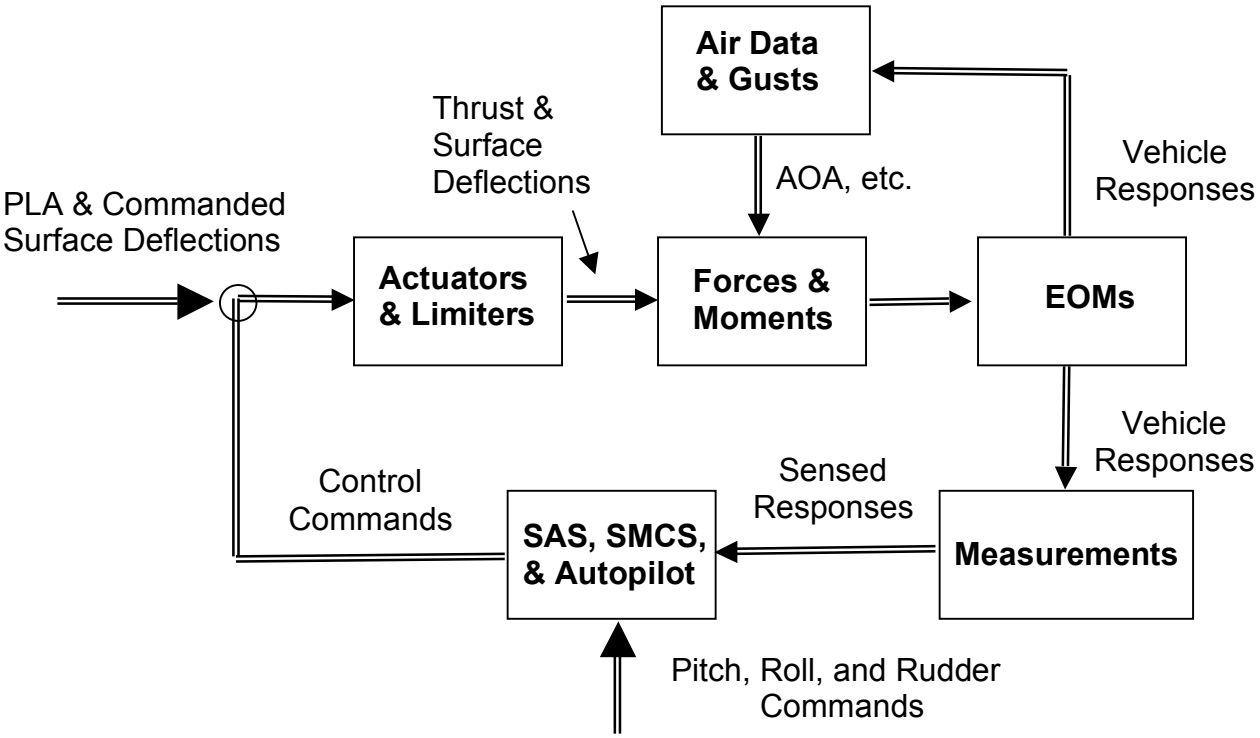

Figure A.1, Block Diagram of The Simulation

The Simulation includes an extensive array of stochastic and deterministic inputs, including pitch, roll, and rudder commands selected by the user to command the system These three inputs are the primary vehicle-control inputs, and would have originated from the cockpit stick and rudder pedals. But these cockpit effectors are not modeled in The Simulation. In addition, input ports are provided that allow the user to directly command engine thrust and all surface actuators from the MATLAB workspace, if desired. These input ports are included to

allow analysis of the dynamics of The Simulation, for example. Finally, an extensive array of output ports is also included to allow for export and recording of key vehicle responses and states. A list of all simulation inputs and outputs is given in Table A.1.

Table A.1, Deterministic Inputs and Output Ports Available In The Simulation

Inputs	**Port No.**	**Outputs**	**Port No.**
Pitch Command, deg	*	Inertial Surge Velocity U, fps	1
Roll Command, deg	*	Inertial Lateral Velocity V, fps	2
Rudder Command, deg	*	Inertial Plunge Velocity W, fps	3
Engine Power-Lever Angle δ_{PLA}, deg	1	Roll Rate (rigid-body), P deg/s	4
Horizontal Tail (sym), δ_{Hc} deg	2	Pitch Rate (rigid-body), Q deg/s	5
Horizontal Tail (anti-sym), δ_{DHc} deg	3	Yaw Rate (rigid-body), R deg/s	6
Rudder (upper), δ_{RUc} deg	4	Roll Euler Angle, ϕ deg	7
Rudder (lower), δ_{RLc} deg	5	Attitude Euler Angle, θ deg	8
Spoiler, $\delta_{sp\,c}$ deg	6	Heading Euler Angle, ψ deg	9
Control Vanes (anti-sym), $\delta_{cv\,anti\,c}$ deg	7	Air Speed, $V_{\infty\,a}$ fps	10
Control Vanes (sym), $\delta_{cv\,sym\,c}$ deg	8	Angle of Attack, α deg	11
		Sideslip Angle, β deg	12
		Altitude, h ft	13
		Flight-Path Angle, γ deg	14
		Roll Rate (c.g.), P_{cg} deg/s	15
		Pitch Rate (c.g.), Q_{cg} deg/s	16
		Yaw Rate (c.g.), R_{cg} deg/s	17
		Lateral Accel. (c.g. rig.-body) $n_{Y\,cg\,RB}$ ft/s/s	18
		Lateral Accel. (c.g.), $n_{Y\,cg}$ ft/s/s	19
		Lateral Accel. (cp), $n_{Y\,cp}$ ft/s/s	20
		Plunge Accel.** (c.g. rig.-body) $n_{Z\,cg\,RB}$ ft/s/s	21
		Plunge Accel.** (c.g.), $n_{Z\,cg}$ ft/s/s	22
		Plunge Accel.** (cp), $n_{Z\,cp}$ ft/s/s	23

* These inputs are pre-defined, and part of The Simulation.
** Plunge Acceleration Relative to 1-g trim

The steps necessary to set up a simulation are as follow:

1. Open the Simulink model file FLEXSIM.slx
2. Load the data file FSdata.mat into the MATLAB workspace.

3. Assure that the initial conditions on the integrators are set to the correct values.
4. Assure that the trim PLA and horizontal-tail deflection are set to the correct values.
5. Select the desired inputs to excite the simulation (e.g., gusts, control commands).
6. Activate or de-activate the feedback-control systems (i.e, SAS's and SMCS's), as desired.
7. Open the Model Configuration Parameters dialog box in the Simulink model window.
8. Click on Solver in the left panel, and set the desired simulation stop time.
9. Click on Import/Export in the left panel, and assure that the desired model outputs (e.g., tout and yout) will be exported to the MATLAB workspace, if desired. Close the dialog box.
10. Click on Run, to execute. Click either the Run button along the top of the model window, or click on Run in the pull-down menu under Simulation.
11. By default, all the simulation responses are written to a file called yout, along with the corresponding simulated time in tout. The columns in yout correspond to the numbered and labeled output tabs shown in the Simulink model window.

The data file FSdata.mat contains the engine database, the vehicle's mass and inertia properties, and the parameters *S, b,* and $\bar{c}$ used in the aerodynamic force and moment models. None of these parameters should ever be changed. The remaining data in this file may be changed if desired. These three parameters include the two that define the gust spectra, or U0gust and sigmag, and the one defining the in-vacuo modal damping ζ (zeta) of the free-vibration modes used to build the aeroelastic models. As discussed in Section 6 when describing the gust models, by default U0gust and sigmag are set to 659 fps and 6 fps, respectively. If the user wishes to change the gust spectra, he/she may do so by adjusting these two parameters. Also by default, the vibration-modal damping zeta is set to the default value of 0.02. The user may adjust this parameter as well, if the experiment requires doing so. But it should never exceed about 0.06.

The initial conditions on all integrators in The Simulation must be set prior to execution, and all integrators have labels as indicated in the model window. However, most of these initial conditions will remain at their default values of zero. Those that must typically be set to non-zero values are listed in the Initial-Condition Table, Table A.1. The seven integrators that must be set, along with the subsystems containing these integrators, are highlighted in red in The Simulation

model window for ease of identification. These initial conditions are set according to the user-selected initial trim flight conditions are changed over the flight envelope described in Section 9. Trim initial condition outside this flight envelope should not be used.

Table A.1, Initial-Condition Table

Altitude, ft	5000	5000	5000	20000	20000	20000	30000
Mach	0.8	0.6	0.5	0.8	0.7	0.6	0.75
U int, fps	876.610	658.950	547.385	829.346	724.760	617.380	740.659
W int, fps	-43.277	8.226	35.739	12.480	38.041	76.326	89.025
theta int, rad	-0.04933	0.01248	0.06520	0.01500	0.05244	0.12300	0.11961
h int, ft	5,000	5,000	5,000	20,000	20,000	20,000	30,000
E1 int	1.69030	0.60827	0.26742	0.58467	0.32856	0.08726	0.09538
E2 int	0.06896	0.04342	0.03962	0.04307	0.04007	0.04133	0.04114
E3 int	-0.10040	-0.05531	-0.03850	-0.05420	-0.04165	-0.03063	-0.03092
$delH_{trim}$ deg	-5.548	-6.616	-8.117	-6.685	-7.742	-9.890	-9.784
PLA_{trim}, deg	72.999	66.341	60.094	87.894	72.975	84.528	93.474

The trim settings on PLA and horizontal-tail deflection must also be set, corresponding to the initial trim flight condition selected by the user. These trim values are also listed in the last two rows of the Initial-Condition Table, Table A.1. One tip - after setting the initial conditions and control inputs for trim, it is suggested that the user simulate 10-15 seconds with no commands or gusts exciting the system, to verify that trim was actually achieved. The Simulink blocks that must be modified to establish these trim settings are highlighted in red in The Simulation model window.

The system excitations that may be selected include atmospheric turbulence, pitch SAS command, roll SAS command, and rudder SAS command. Individual control surfaces may also be actuated using inputs from the MATLAB workspace, if desired. Vertical and/or horizontal turbulence are activated by double clicking on the manual switches, highlighted in green, in the AirData-Gusts/TurbulenceModel subsystem. A negative-one-degree, five-second doublet may be commanded for horizontal-tail deflection by double clicking on the manual switch, highlighted in green, located in the bottom-left quadrant in the model window at the root level of The Simulation. Likewise a one-degree, five-second doublet may be input to the SAS roll- and/or rudder-command by double clicking on the manual switches, highlighted in green, also located in the bottom-left quadrant of the model window at the root level of The Simulation. If other

inputs are to be used, the user must modify the Simulink model accordingly.

The user may also select the SAS's and SMCS's that are active or inactive. This is accomplished by double clicking on the appropriate manual switch, highlighted in green. These switches are in the subsystems located in the SAS/SMCS Systems subsystem, located in the lower left quadrant of the root-level simulation diagram. Now The Simulation is ready for execution.

Several example test cases will now be presented. The simulation configurations being considered are tabulated in Table A.2. The first case was run at the default flight condition, with all feedback systems active as noted in Table A.2. The vertical- and lateral-acceleration (c.p.), horizontal-tail, differential-tail, spoiler, lower-rudder, and right- and left-control-vane responses to the combined pitch and roll doublets are shown in Figs. A.2–A.9, respectively.

Table A.2, Simulation Configurations for Test Cases

FC Default M = 0.6, *h* = 5000 ft. SAS – all on SMCS – all on Excitation – Pitch plus Roll-Command 1-deg Doublets	
FC 1, Case 1, M = 0.8, *h* = 5000 ft. SAS – all off or Pitch SAS Only On SMCS – all off or Vertical SMCS On Excitation – Pitch -1-deg Doublet	*FC* 1, Case 2 M = 0.8, *h* = 5000 ft. SAS – all off or Roll & Yaw SAS On SMCS – all off or Lateral SMCS On Excitation – Roll-Command 1-deg Doublet
FC 2, Case 1 M = 0.5, *h* = 5000 ft. SAS – all off or Pitch SAS Only On SMCS – all off or Vertical SMCS On Excitation – Pitch -1-deg Doublet	*FC* 2, Case 2 M = 0.5, *h* = 5000 ft. SAS – all off or Roll & Yaw SAS On SMCS – all off or Lateral SMCS On Excitation – Roll-Command 1-deg Doublet

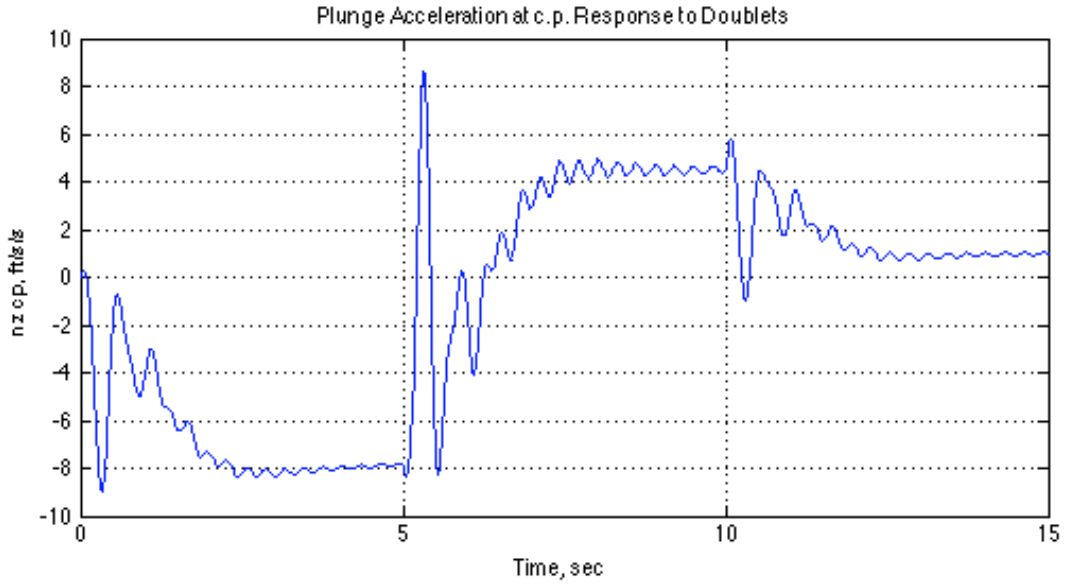

Figure A.2, Plunge-Acceleration Response to Pitch+Roll Doublets

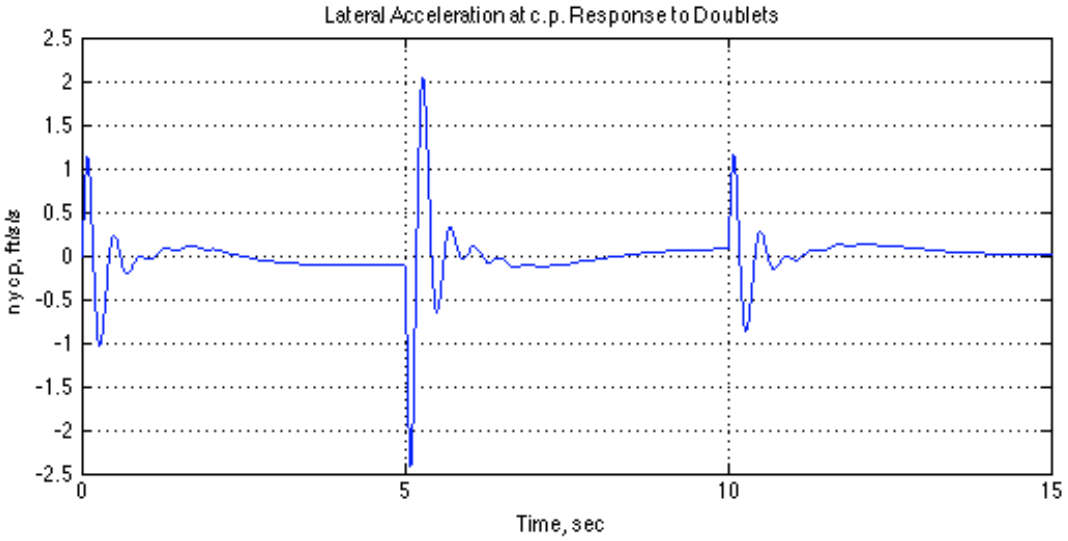

Figure A.3, Lateral-Acceleration Response to Pitch+Roll Doublets

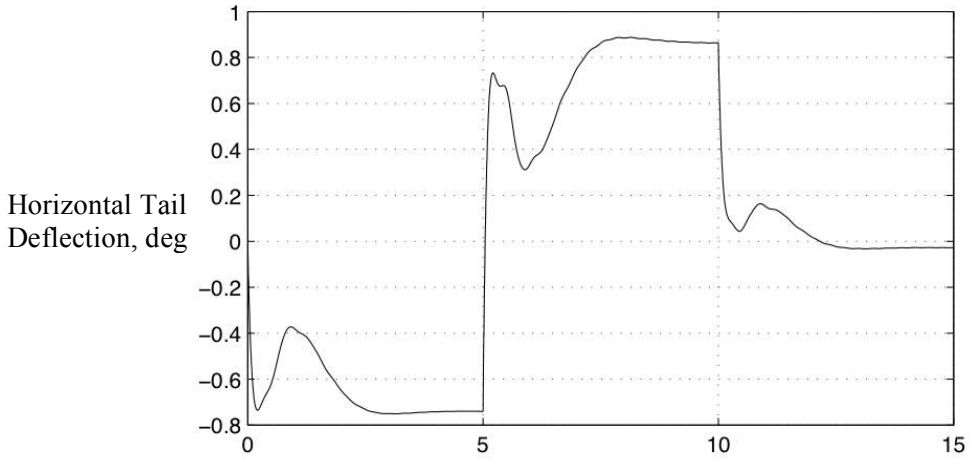

Figure A.4, Symmetric-Horizontal-Tail Response to Pitch+Roll Doublets

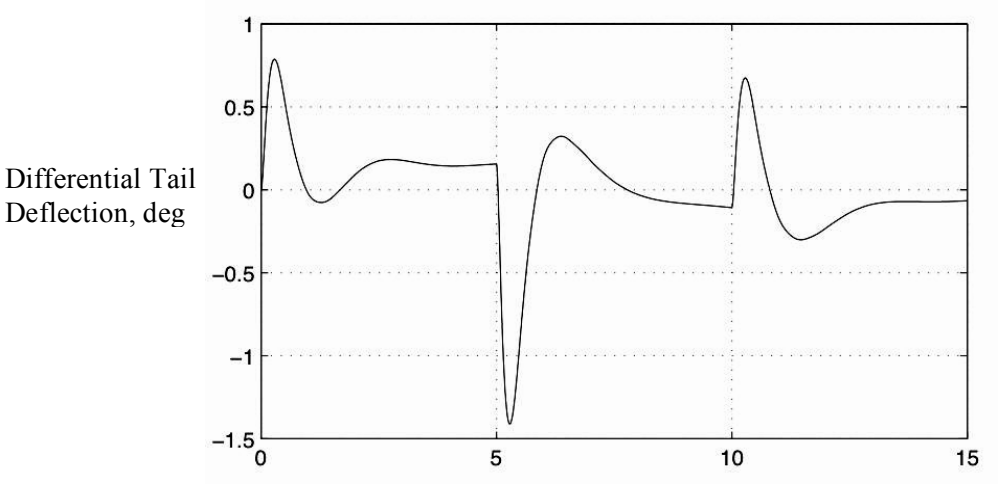

Figure A.5, Differential-Stabilizer Response to Pitch+Roll Doublets

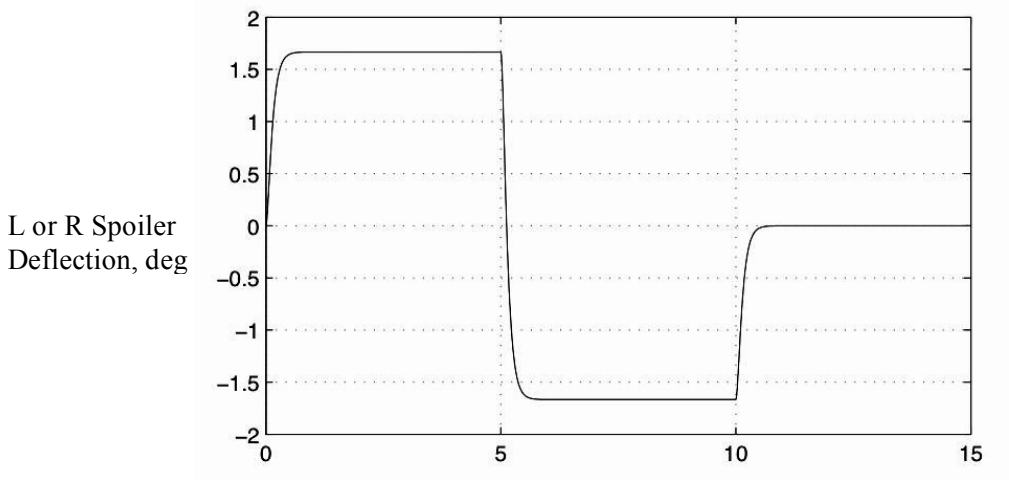

Figure A.6, Spoiler Response to Pitch+Roll Doublets

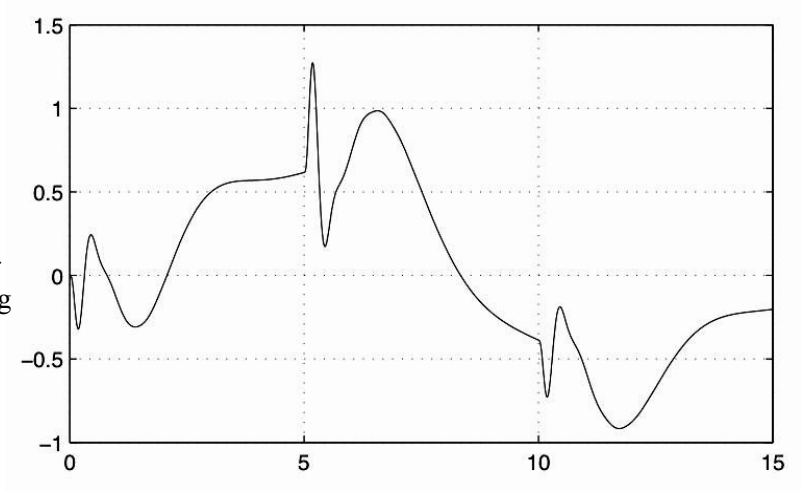

Figure A.7, Lower-Rudder Response to Pitch+Roll Doublets

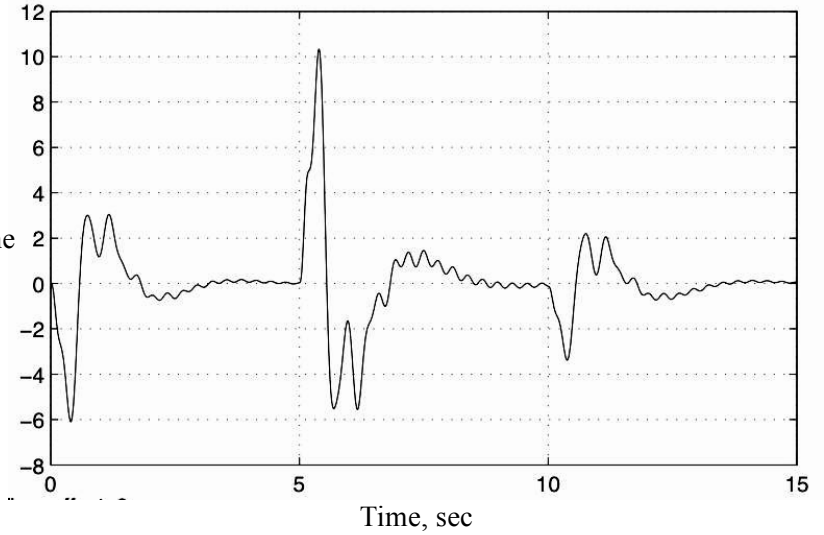

Figure A.8, Right-Control-Vane Response to Pitch+Roll Doublets

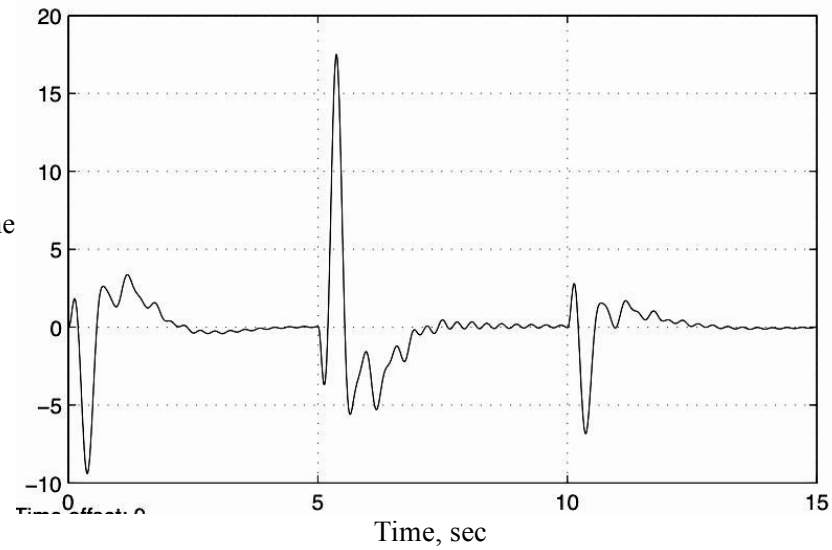

Figure A.9, Left-Control-Vane Response to Pitch+Roll Doublets

Next, consider Flight Condition 1. The highest trim dynamic pressure will be experienced in this flight condition. For the configurations defined in Case 1, the excitation is the negative-one-degree pitch doublet only. This is an aggressive input at this dynamic pressure. The pitch-rate (c.g.) responses (with SMCS's off) with and without the pitch SAS active are shown in Fig. A.10, while the vertical-acceleration (c.p.) responses (with pitch SAS on) with and without the vertical SMCS active are shown in Fig. A.11.

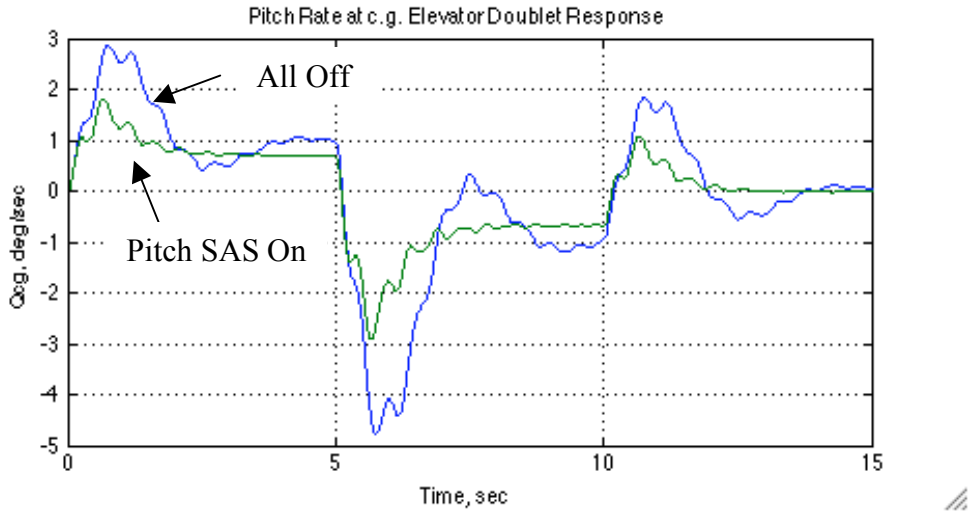

Figure A.10, Pitch-Rate (c.g.) Responses to Pitch Doublet (FC 1)

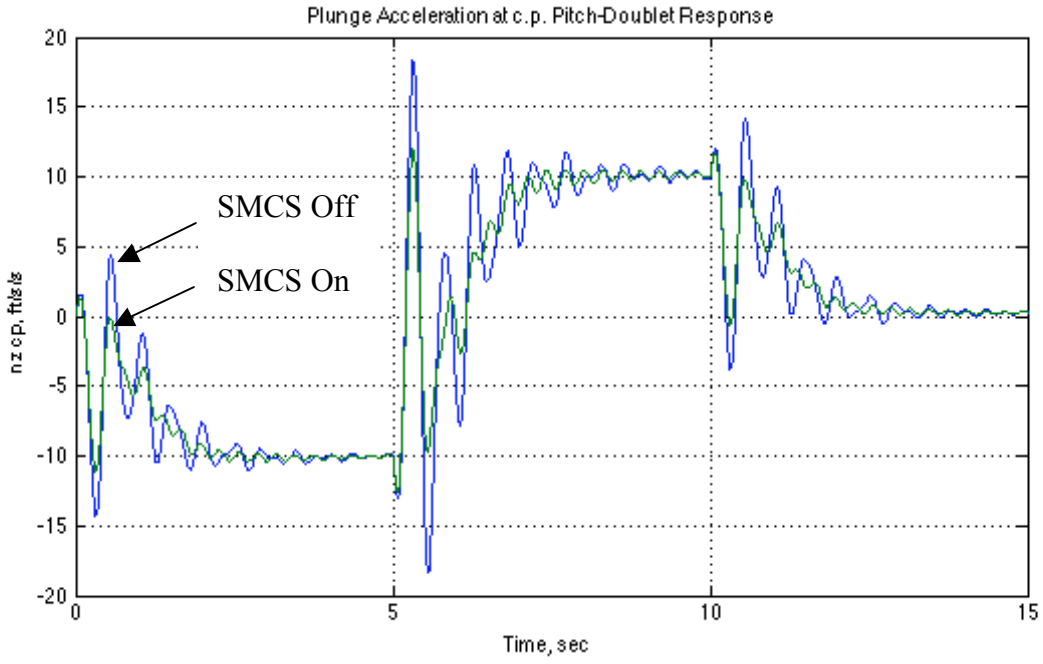

Figure A.11, Plunge-Acceleration (c.p.) Responses to Pitch Doublet (FC 1)

Again considering Flight Condition 1, we'll now look at the configurations defined in Case 2. The excitation is the one-degree roll-command doublet only. This is also an aggressive input at this dynamic pressure. The roll-rate (c.g.) responses (with SMCS's off) with and without the roll and yaw SASs active are shown in Fig. A.12, while the lateral-acceleration (c.p.) responses (with roll and yaw SASs on) with and without the lateral SMCS active are shown in Fig. A.13.

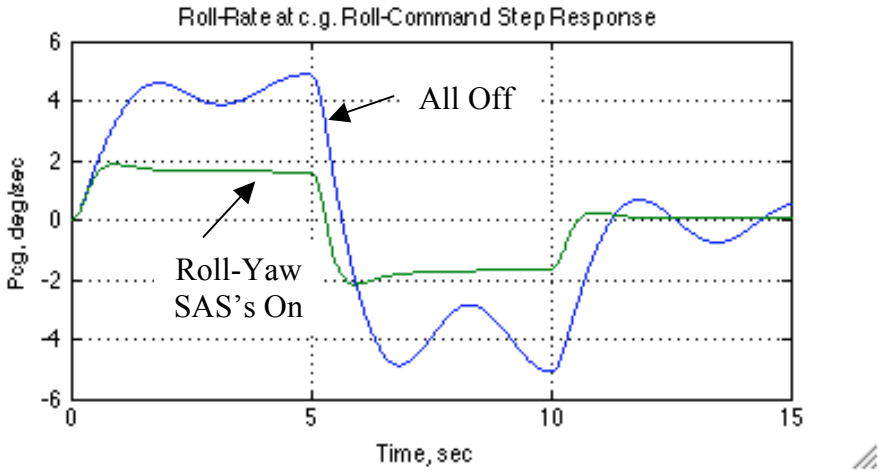

Figure A.12, Roll-Rate (c.g.) Responses to Roll-Command Doublet (FC 1)

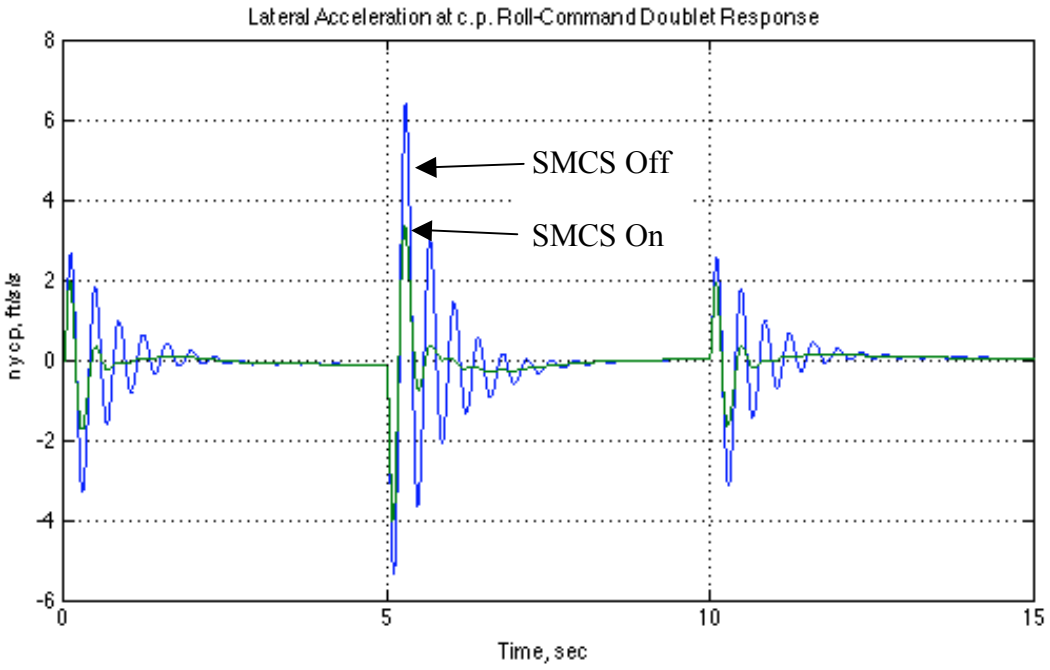

Figure A.13, Lateral-Acceleration (c.p.) Responses to Roll-Command Doublet (FC 1)

Next, consider Flight Condition 2. One of the lowest trim dynamic pressures will be experienced in this flight condition. For the configurations defined in Case 1 for this flight condition, the excitation is the negative-one-degree pitch doublet only. The pitch-rate (c.g.) responses (with SMCS's off) with and without the pitch SAS active are shown in Fig. A.14, while the vertical-acceleration (c.p.) responses (with pitch SAS on) with and without the vertical SMCS active are shown in Fig. A.15.

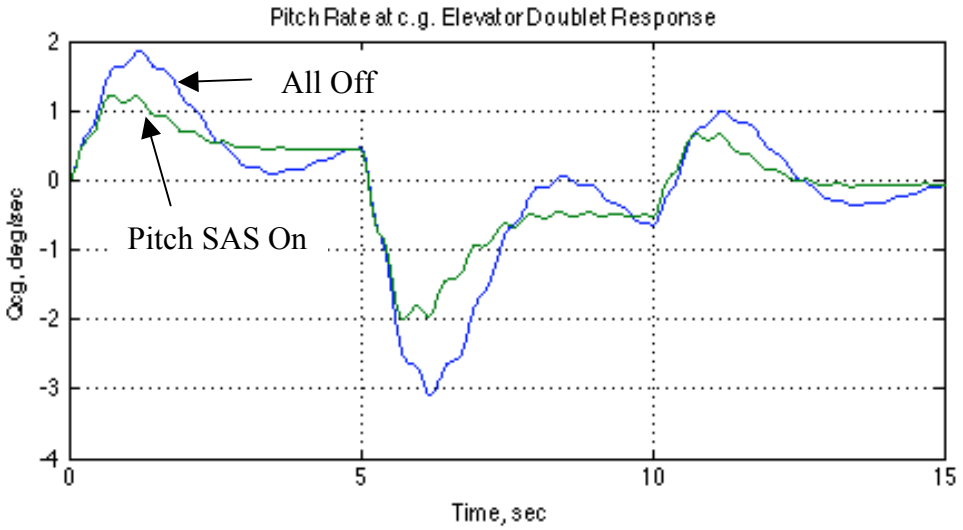

Figure A.14, Pitch-Rate Responses to Pitch Doublet (FC 2)

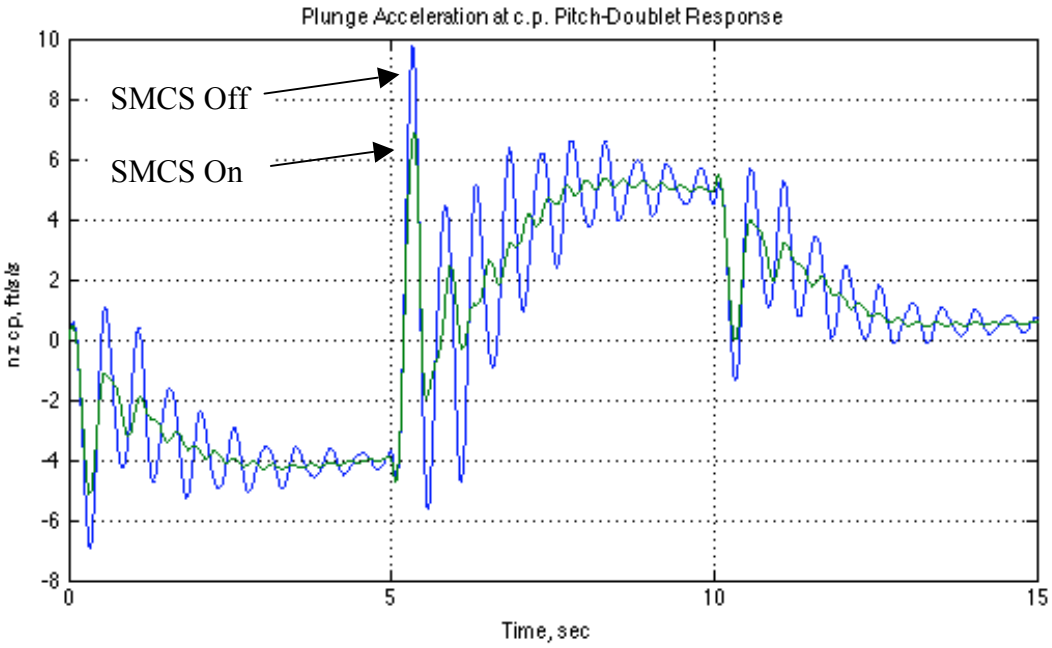

Figure A.15, Plunge-Acceleration (c.p.) Responses to Pitch Doublet (FC 2)

Again considering Flight Condition 2, we'll now look at the configurations defined in Case 2. The excitation is the one-degree roll-command doublet only. The roll-rate (c.g.) responses (with SMCS's off) with and without the roll and yaw SAS's active are shown in Fig. A.16, while the lateral-acceleration (c.p.) responses (with roll and yaw SAS's on) with and without the lateral SMCS active are shown in Fig. A.17.

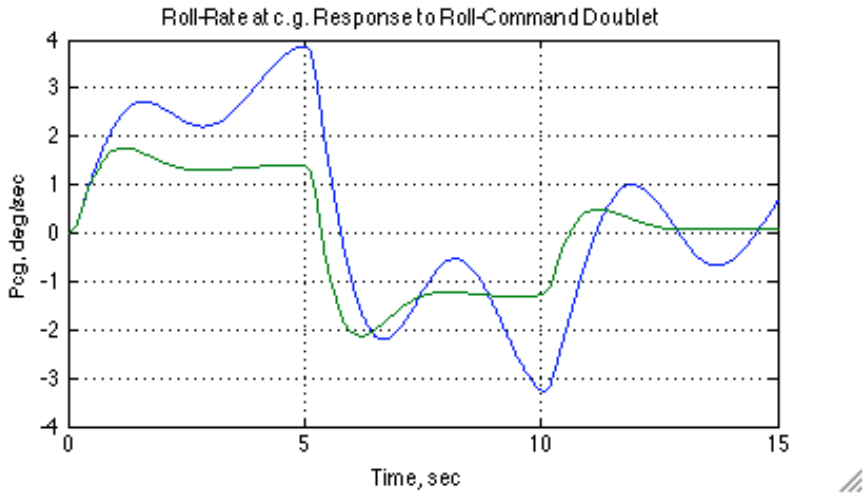

Figure A.16, Roll-Rate Response to Roll-Command Doublet (FC 2)

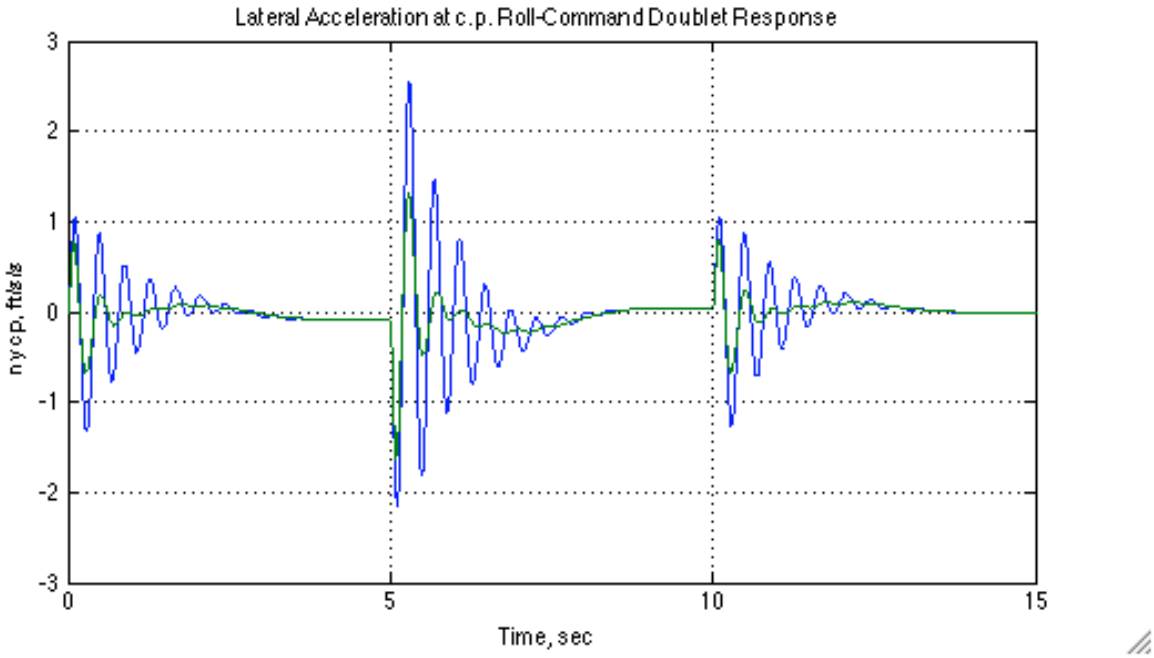

Figure A.17, Lateral-Acceleration (c.p.) Response to Roll-Command Doublet (FC 2)